



UNIVERSITÀ DEGLI STUDI DI ROMA TOR VERGATA

MACROAREA DI SCIENZE MM. FF. NN.

CORSO DI LAUREA IN FISICA

**Purity control of the XENON1T gas
inventory prior to initial filling and
studies of mixing properties of
impurities in gaseous xenon**

MASTER THESIS IN PHYSICS

INTERNAL SUPERVISOR:
**Professor
Roberta Sparvoli**

CANDIDATE:
Veronica Pizzella

EXTERNAL SUPERVISOR:
**Professor
Manfred Lindner**

ACADEMIC YEAR 2015/2016

Abstract

Dark matter composes 27% of the universe but its presence is inferred only from gravitational phenomena. Direct detection experiments, such as XENON1T, attempt to detect the scattering of dark matter particles with the detector target, in this case xenon nuclei. The experiment XENON1T employs 3.3 tonnes of liquid xenon in a Time Projection Chamber (TPC). The TPC is a detector that employs electromagnetic fields in a sensitive volume for 3-d position reconstruction and particle identification. Since dark matter scattering is a rare event, it is necessary to reduce the background to improve the sensitivity of the detector. It is necessary to monitor two kind of impurities in liquid xenon: radioactive impurities such as krypton (present in commercially available xenon at ppb level), since it increases the background, and electronegative molecules such as oxygen and water, since they lower the electron life-time and disrupts the well functioning of the TPC. In this work, the measurements of the xenon inventory prior to filling is presented using the technique of gas chromatography. Some of the bottles measurements are presented and the total purity is summarized. In the second part, a study of gas mixing as solution of inconsistency measurements in the previous part is presented, and different solutions to speed up the gas diffusion are tested. Finally, since gas chromatography is not sensitive to helium, a measurement of the helium concentration in the full xenon inventory is presented using the technique of mass spectrometry.

Contents

1	Dark Matter	3
1.1	Dark matter evidence	3
1.1.1	Star rotational velocities	3
1.1.2	Gravitational lensing	5
1.1.3	Cosmological evidence	6
1.1.4	Large scale structure	7
1.2	Observation explanations	9
1.2.1	Modified Newtonian Dynamics	9
1.2.2	Standard model particles	10
1.2.3	WIMPs	12
1.3	WIMP detection	14
1.3.1	WIMP Production	15
1.3.2	Indirect Detection	15
1.3.3	Direct detection	16
2	The XENON experiment	21
2.1	Liquid xenon as scattering target	21
2.2	XENON detectors principle	22
2.2.1	Dual phase TPC and background discrimination	22
2.2.2	XENON1T detector design	25
2.3	Background of XENON1T	26
2.3.1	External background	26
2.3.2	Internal background	27
2.4	Subsystems	28
2.4.1	ReStoX	29
2.4.2	Xenon Bottle Rack	30
3	Gas purity measurement of xenon	35
3.1	Motivation	35
3.2	Gas chromatography	36
3.2.1	Introduction to gas chromatography	36

3.2.2	Experimental setup	37
3.2.3	Calibration gas	41
3.3	Procedure	41
3.3.1	Background and Calibration	41
3.3.2	Xenon	42
3.4	Analysis	43
3.5	Results	44
3.5.1	Total amount of impurities	45
3.5.2	Measurements of high air contamination	47
3.6	Conclusion	49
4	Gas mixing measurements	51
4.1	Theoretical background	51
4.2	Experimental setup	54
4.3	Procedure	56
4.4	Analysis	57
4.5	Results	61
4.5.1	Argon test	61
4.5.2	Xenon test	65
4.6	Conclusion	69
5	Measurement of helium	71
5.1	Experimental setup	71
5.2	First measurement	72
5.3	Measurement after distillation	75
A	Tables	79
B	Mass Spectrometry	81
	Bibliography	85
	Acknowledgement	89

Chapter 1

Dark Matter

For a long time, gravity has been used as an alternative way to electromagnetic interaction to investigate the universe. If predictions of velocity and distance of stars and other celestial bodies do not match expectations from the gravitational laws, either the gravitational theory is not correct or there are additional, not yet observed masses. For example in 1840, J. C. Adams and U. Le Verrier calculated the presence of an eighth planet of the solar system based on the perturbations of the orbit of Uranus. Assuming that Kepler's laws were correct, they deduced the presence of another planet, which was later observed by J. G. Galle and now is called Neptune.

The first hint towards unobserved masses was found by Fritz Zwicky in 1933. Zwicky measured the mass of the Coma galaxy cluster using the Doppler effect to measure the velocities of the galaxies and then used the virial theorem to compute the total mass. Comparing this result to the visible mass, he saw that the two results were not in agreement [1]. Assuming that the virial theorem is correct, he deduced that most of the mass in the cluster does not emit light. The unknown no light emitting matter was named "dark matter".

1.1 Dark matter evidence

After the first observation by Zwicky, other ones indicate the possibility of the presence of dark matter. In this section, additional important evidence is presented.

1.1.1 Star rotational velocities

One of the first observed evidence for dark matter is the distribution of rotational velocities of stars in a spiral galaxy. The dependence of a star velocity from its

distance from the galactic center r as derived from Newton's law is

$$v(r) = \sqrt{\frac{GM(r)}{r}} \quad (1.1)$$

where $M(r) = 4\pi \int \rho(r) r^2 dr$ is the mass at that distance. For a spiral galaxy, most of the visible mass is concentrated in the bulge at the center of the galaxy. Assuming that $M(r)$ is constant outside the core of the galaxy, we expect $v(r) \propto r^{-1/2}$. However velocity measurements indicate a flat distribution [2]. In order to have a constant velocity, a mass distribution $\rho(r) \propto r^{1/2}$ is needed (see figure 1.1).

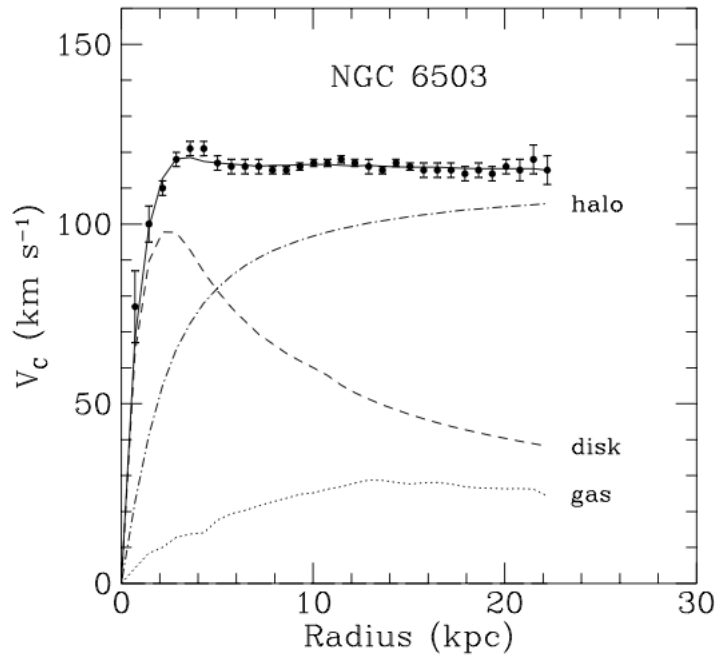


Figure 1.1: Velocity distribution of NGC 6503. The black dots are the observed velocities, while the dashed line is the expected profile from the visible matter. The dotted line is the contribution of gas and the dashed-dotted line is the total contribution needed to have the observed velocity distribution. Figure taken from [2].

To achieve the observed star velocity profile, there must be a matter halo enclosing the galaxies. Since the visible mass does not follow a halo profile, it must be composed of dark matter to a great extent.

1.1.2 Gravitational lensing

Gravitational lensing is the effect of the distortion of space-time caused by mass concentrations, which leads to a distorted path of the photons that travel next to the mass concentration [3, Ch. 4]. For so called strong gravitational lensing, multiple ghost images of the source are generated. For weak or micro-lensing, there is a time modulation of the light intensity, due to the motion of the lensing object. This effect has been used to measure the mass of different celestial objects.

One of the initial hypotheses about the missing mass in galaxies is the presence of Massive Compact Halo Object (MACHOs). A MACHO is a massive object which emits little to no radiation, thus making it hard to impossible to detect. MACHOs include black holes, neutron stars and brown dwarves. Since they emit little to no light, weak gravitational lensing is used to estimate their mass. For example the MACHO project [4] studied the Magellanic Cloud and counted the MACHOs objects inside. They found that for a typical MACHO model, the contribution of MACHOs to the total dark matter mass is about 20%, with 95% confidence that it is between 8% and 50% [4]. A 100% MACHO dark matter distribution is excluded.

Another application of gravitational lensing is the study of the bullet cluster (1E 0657-558) [5]. A cluster is composed of the galaxies and intragalactic plasma, which is an X-rays emitter. The bullet cluster is the result of a collision of two separate clusters. According to observations, it is expected that the plasma is the dominant mass component of a cluster. In a collision of two clusters, the galaxies act as collisionless particles while the plasma from the two galaxies slows down due to electromagnetic interaction. The result is the decoupling of the galaxies from the plasma, which can be seen in figure 1.2a.

Using weak gravitational lensing, it is possible to reconstruct the mass profile of the bullet cluster. The expectation is that the gravitational potential follows the plasma profile since it is the dominant mass component. In figure 1.2b we see, however, that the centers of mass of the two clusters (indicated by the green lines) correspond to the one of the galaxies from figure 1.2a, and not to the plasma profile (yellow in figure 1.2b).

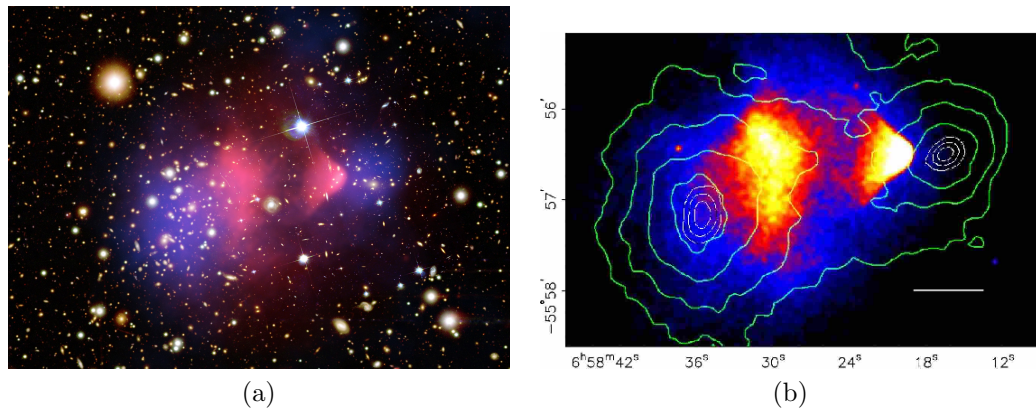


Figure 1.2: On the left: artistic image of the bullet cluster [6]. On the right: bullet cluster in X-rays from Chandra. The green lines indicates the mass distribution reconstructed from weak gravitational lensing. Figure taken from [7].

The conclusion is that the plasma is not the dominant massive component. The actual dominant component does not emit light and is what we call dark matter. The reason of the shift of the center of gravity is that dark matter and baryonic matter do not interact in the same way: while baryonic matter slows down due to scattering effects, dark matter does not interact neither with baryonic matter nor with itself. The result is that dark matter crosses the cluster as if it is transparent, while the plasma falls behind.

1.1.3 Cosmological evidence

The Cosmic Microwave Background (CMB) is the radiation of relic photons from the last scattering surface of the Big Bang. The CMB is mostly an isotropic emission and with the spectrum of a black body with a temperature of 2.726 K [8]. However, there are small anisotropies with an order of magnitude of 10^{-5} K [9]. The power spectrum of the CMB (figure 1.3) shows that there is a structure in the anisotropies.

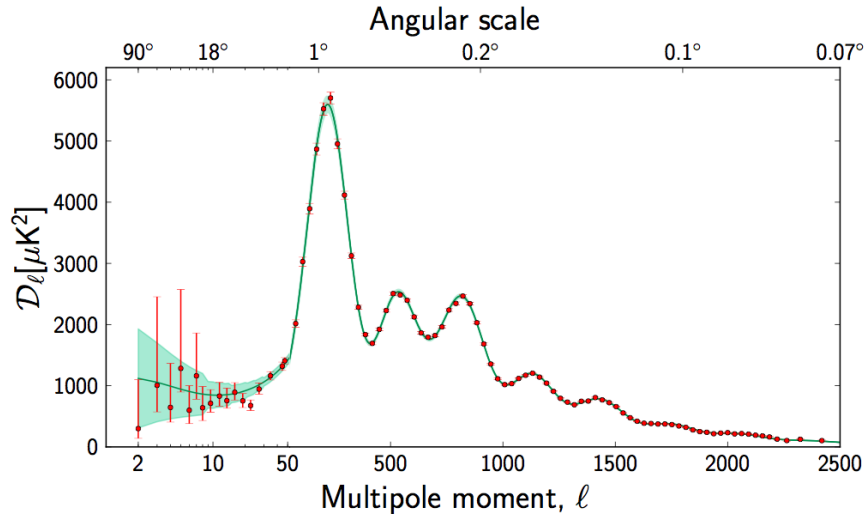


Figure 1.3: Temperature angular power spectrum of the primary CMB from Planck [10], showing a precise measurement of seven acoustic peaks measure that are well-fitted by a six-parameter Λ CDM model.

To explain the peaks in the CMB spectrum, the Λ CDM model is used. This model introduces dark energy (Λ) and cold dark matter CDM (explained in section 1.2.2) to parameterize the evolution of the universe and has 6 free parameters, among them being the density of baryons (Ω_b), dark matter (Ω_{DM}) and dark energy (Ω_Λ). From the fit of the power spectrum, the dark matter contribution to the total universe mass is 27 – 28%.

This result is compared with the density of baryons expected from the Big Bang Nucleosynthesis (BBN), the creation of light elements (helium, deuterium and traces of lithium) in the early universe [3, Ch. 28]. Studying the ratio of elements, it is possible to set limits on Ω_b . The result is $0.017 \geq \Omega_b \geq 0.024$ at 95% confidence level [11].

1.1.4 Large scale structure

While the anisotropies of the CMB are small, the universe we see today is not isotropic at a small scale. The galaxies and the matter inside the galaxies are distributed in large scale structures, and we can assume that also dark matter has formed structures. The evolution of large scale structures is a process driven by the gravitational force and is highly non-linear. Since it is hard to calculate analytically, the best way to predict the evolution is through numerical simulation [12]. The simulation uses the Λ CDM model and assumes it is possible to describe dark matter as an N-body simulation. The key features of the simulation are:

- only gravitational force;
- collision less dark matter;
- baryonic matter with large scale structures at the time of the Big Bang and at present day;
- dark matter isotropic at the time of the Big Bang, but with large scale structures at present day;
- baryonic structures growth in the dark matter halos;
- condensation of baryonic matter and creation of stars.

Figure 1.4 gives a visual representation of the simulation. It can be seen that at higher redshift (z), which corresponds to times farther in the past, galaxies are already clustered while dark matter is distributed more homogeneously. As time evolves, dark matter assumes the same structures as baryonic matter.

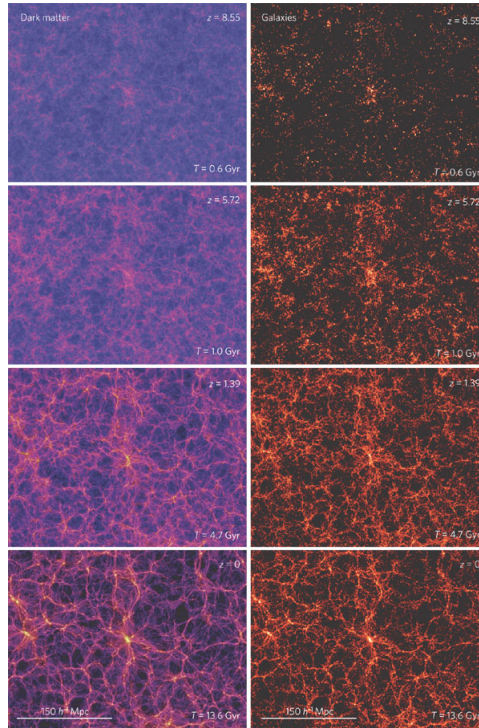


Figure 1.4: Projected dark matter distributions from Millennium N-body simulations. On the left dark matter is displayed, on the right baryonic matter. The epochs displayed correspond to 600 million, 1 billion, 4.7 billion and 13.6 billion (today) years after the Big Bang. Figure taken from [12].

There are two main problems which have arisen from the simulations. The first one is that the simulation predicts many small dark matter substructures inside the galaxy haloes, which are not observed. This may be simply due to the fact that the calculation of the distribution of dark matter inside a galaxy is not sensitive enough given the means we have at the moment. The second problem is that the Λ CDM model predicts cusp-core density profiles for dark matter (a profile that features a lot of mass in the middle), which is not supported by the star velocity profile. One possible reason is that the simulations so far have not considered baryonic matter.

1.2 Observation explanations

There are different theories that aim to explain the discrepancies between visible matter and matter calculated with the laws of gravitation. The first one described in this section attempts to explain it without assuming extra mass. Afterwards, the most endorsed theories at present is explained, the one which states that dark matter has a particle nature.

1.2.1 Modified Newtonian Dynamics

Modified Newtonian Dynamics (MOND) is a theory that first attempts to explain velocity profiles of the stars in a galaxy [13]. The idea of this theory is that the gravitational laws and general relativity are not valid outside the solar system, in the approximation of large distances and low mass where the gravitational potential is

$$\Phi = \frac{MG}{r} \ll c^2 \quad (1.2)$$

MOND introduces a new constant, a_0 , that has the dimensions of an acceleration and modifies the force equation

$$F = m\mu\left(\frac{a}{a_0}\right)a \quad (1.3)$$

where

$$\mu(x) = \begin{cases} 1, & \text{if } x \gg 1 \\ x, & \text{if } x \ll 1 \end{cases} \quad (1.4)$$

In the limit of $x \gg 1$, which means $a_0 \rightarrow 0$, newtonian dynamics are restored. In the opposite case, when $x \ll 1$ or deep MOND approximation, equation 1.3 becomes

$$F = m\frac{a^2}{a_0} \quad (1.5)$$

Applying this equation to a body on a circular orbit gives

$$F = \frac{GmM}{r^2} = m\frac{(v/r)^2}{a_0} \implies v^4 = GMa_0 \quad (1.6)$$

Thus the velocity does not depend anymore on the radius, in agreement with astronomical observations. In this model, a_0 is a universal constant and should be the same for all galaxies. A way to check the validity of this theory is to fit the velocity of stars in different galaxies and compare the values obtained for a_0 . It has been observed that there is a weak correlation between a_0 and the central surface brightness of a galaxy [14]. This is a problem for a MOND scenario, since a_0 is supposed to be an universal constant.

1.2.2 Standard model particles

Since the MOND theory can not explain all evidence, the most endorsed hypothesis is that dark matter is made up by particles. We can outline the following properties that the particles must have to fit with all the observations:

- massive: it has to interact through gravity;
- neutral electric charge: it can not interact through electromagnetic force;
- neutral color charge: it can not interact through strong force;
- at most, interact through the weak force;
- stable or long-lived: its lifetime must be longer than the age of the Universe.

We can also pose a condition on the energy of dark matter particles. Depending on the velocity of the particle, dark matter is divided in three categories:

- Hot Dark Matter: particles with relativistic speed
- Cold Dark Matter: particles with speed $< 10^{-8}c$
- Warm Dark Matter: particles with an intermediate speed

The observation of large scale structures rules out the hot dark matter, as the particles could not be bound in a structure with this energy. Only cold or warm dark matter are allowed. As stated before, the Λ CDM model assumes cold dark matter.

The first try is to look for a particle with such properties among the 61 particles of the Standard Model (SM).

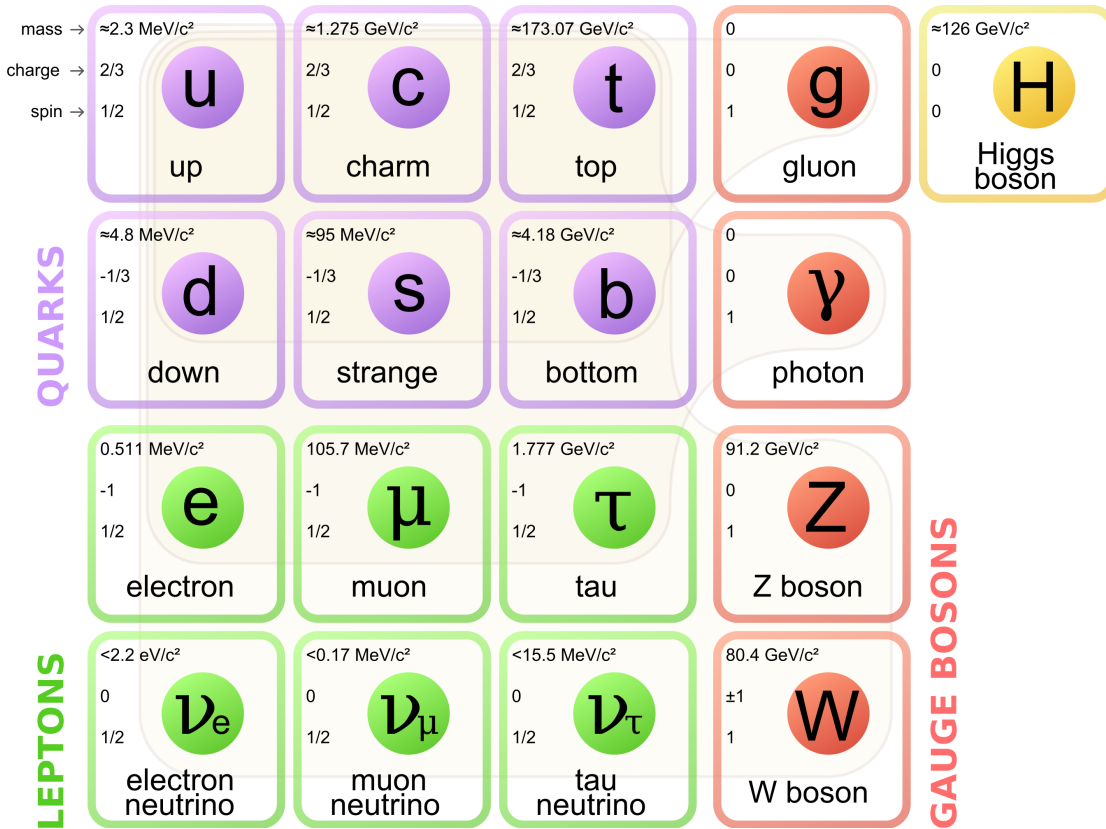


Figure 1.5: The particles of the Standard Model. There are 12×3 quarks, 12 leptons, 12 gauge bosons and the Higgs boson. [15]

There are only two SM particles which fulfill the previously mentioned criteria. The first one is the Higgs boson, but it can not be dark matter since it has a short lifetime. The other ones are the three neutrinos, which were the most probable candidate for a long time. They have all the previously listed properties, and it has been proved through neutrino oscillation that they have mass [16]. However, they can not compose dark matter for two reasons. First, with the current limits on their mass, their relic density is too low. Their phase space does not allow their number density to be enough to account for all the dark matter mass in galaxies. The second point is that even if they would have sufficient mass, they are relativistic particles and would be hot dark matter.

In conclusion, there is no current particle in the SM that can be a dark matter candidate. The candidates must then postulated from particles beyond the standard model.

1.2.3 WIMPs

Weakly Interacting Massive Particles (WIMPs, denoted with letter χ) indicate a class of particles which have all the desired properties and are good candidate for dark matter. In the standard scenario, they were created in the early universe in the radiation dominated era [3, Ch. 7]. At the beginning, all their reactions were at equilibrium with baryonic matter.

$$\chi\bar{\chi} \leftrightarrow e^+e^-, \mu^+\mu^-, q\bar{q}, W^+W^-, ZZ, HH, \dots$$

When the universe expanded, the temperature of the primordial plasma decreased and became smaller than the WIMP mass. Since the particles have a Boltzmann energy distribution, the production reaction could still occur in the high energy tail. The number density of χ decreased as $\exp(-m_\chi/T)$. In addition, the expansion of the universe caused a drop of the number density of particles n_χ . When n_χ was sufficiently low, the reaction rate dropped and there was a “freeze-out” of the particles: the annihilation was so slow that their number is constant. The time of the freeze-out, thus the number density of WIMPs remain-

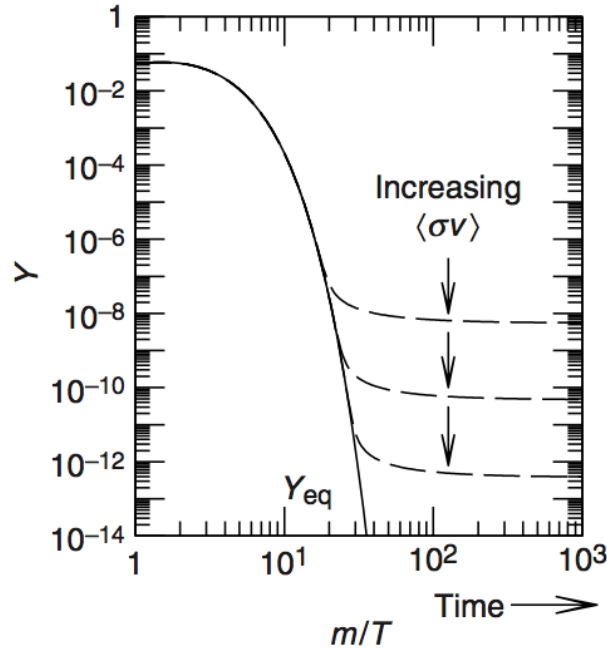


Figure 1.6: Typical evolution of the WIMP number density in the early Universe during the epoch of WIMP chemical decoupling (freeze-out). The x axis is the mass divided by the temperature, and the y axis is $Y = n/s$, the comoving number density. Figure taken from [3, Ch. 7].

ing, is proportional to the average annihilation cross section and the velocity of χ particles ($\langle\sigma_{ann}v_\chi\rangle$). The evolution of n_χ is shown in figure 1.6.

The thermal relic density of the particle χ may be written as [3, Ch. 7]

$$\Omega_\chi h^2 = \frac{\rho_\chi^0 h^2}{\rho_c^0} = \frac{3 \times 10^{27}}{\langle\sigma_{ann}v\rangle} \text{cm}^3 \text{s}^{-1} \quad (1.7)$$

where $\Omega_\chi = \rho_\chi/\rho_c^0$ and ρ_c^0 is the present critical density. The WIMP ‘‘miracle’’ [3, Ch. 10] is the fact that for masses and cross sections of the order of the weak interaction, Ω_χ has approximately the value we expect for Ω_{DM} from cosmological observations.

Supersymmetry

The supersymmetric theory offers some valid particle dark matter candidates [3, Ch. 8]. This theory states that each SM fermion has a supersymmetric bosonic partner and vice versa (indicated with a tilde). It also introduces a new quantum number, the R-parity, defined as

$$R = (-1)^{3B+L+2S} \quad (1.8)$$

where B is the baryonic number, L the leptonic number and S the spin. With this definition, the SM particles have $R = +1$, while the new Supersymmetric (SUSY) particles have $R = -1$. Since the R-parity is conserved, the Lightest SUSY Particle (LSP) can not decay into a SM particle.

The possible LSP candidates must at most interact weakly, as for all dark matter candidates. Some candidates are:

s-neutrino: it has spin = 0 but it is excluded by experimental results [17].

neutralino: it has spin = $\frac{1}{2}$ and it is a combination of different fermionic partners of gauge bosons: $\chi = \alpha\tilde{\gamma} + \beta\tilde{B} + \gamma\tilde{H}_1 + \delta\tilde{H}_2$. This particle also has limits on the cross section but they leave still room below. It is the most promising supersymmetric dark matter candidate.

gravitino: it only interacts gravitationally, so it is not expected to be in thermal equilibrium in the early universe. It can be created by high energy particle collision in the early universe or decay of other susy.

next to lightest particles: there are some candidate particles among the next to the lightest supersymmetric particles (NLSP), even if there are constraint due to their decay into gravitino. Some example are the $\tilde{\tau}$ and \tilde{t} .

1.3 WIMP detection

Even if we do not know the details, we can outline WIMPs (χ) interaction with SM particles. Figure 1.7 shows possible directions of the interaction and the corresponding kinds of searches.

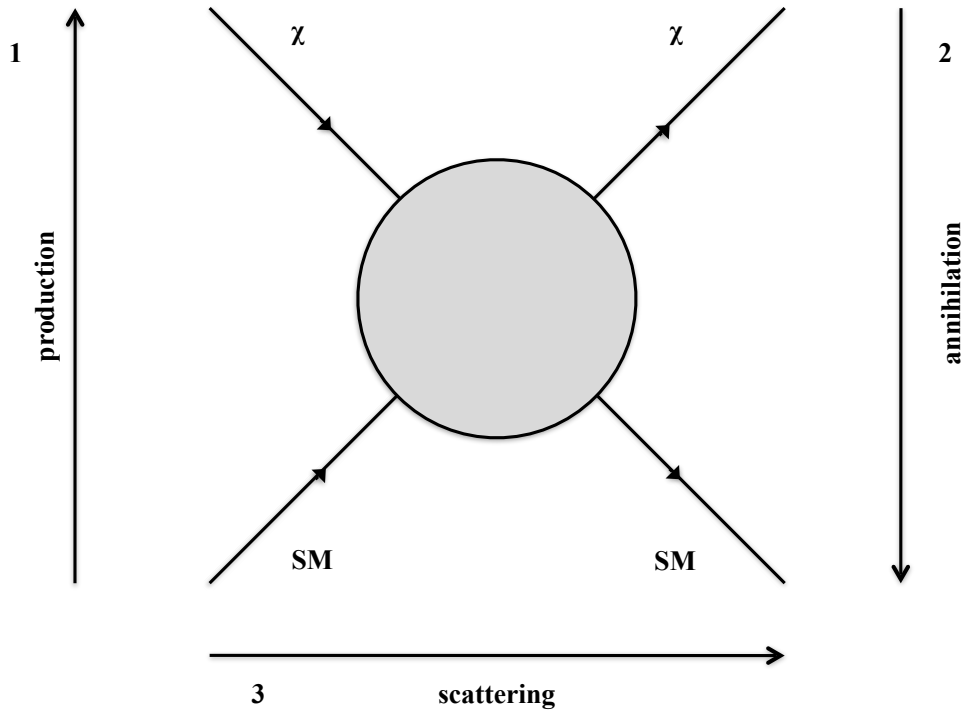


Figure 1.7: Feynman diagram of WIMP-SM particle interaction. The grey circle stands for an unknown interaction. There are 3 directions, indicated by the arrows.

1. WIMPs production: two SM particles collide at high energy generating WIMPs.
2. WIMPs annihilation: if the WIMP density is enough, they can annihilate and create SM particles. The search for these particles is called indirect detection.
3. WIMPs scattering: one can detect the recoil of a SM particle caused by WIMPs. This is called direct detection.

1.3.1 WIMP Production

If dark matter particles interact with SM particles, it is possible to produce dark matter in particle accelerators [18, 19]. However, since they are heavier than SM particles, high energy and luminosity are required. At present time the only particle accelerator that fulfills the requirements is the Large Hadron Collider (LHC), at CERN. The most researched particles as dark matter candidates are LSPs. They can be either produced directly or decay from heavier SUSY particles. Since the cross-section of dark matter interaction with baryonic matter is small, the only way to detect them is via missing energy and momentum. In addition, even if missing energy indicates that SUSY particles are generated, it is impossible to see if they are stable, a requirement for a dark matter candidate.

1.3.2 Indirect Detection

Dark matter can produce SM particles in decay or annihilation reactions. Some possible annihilation reactions could be

$$\begin{aligned} \chi\bar{\chi} &\rightarrow \gamma\gamma, \gamma Z, \gamma H \\ &\rightarrow q\bar{q}, W^+W^-, ZZ \rightarrow e^+e^-, p\bar{p}, \nu s \end{aligned}$$

and decay reactions

$$\chi \rightarrow \psi + \gamma, \psi + \nu$$

where χ and ψ are dark matter particles.

The reaction products can be detected to give a limit on the density of dark matter. Since the secondary particle rate is proportional to the dark matter density, the most abundant flux is expected from high mass celestial bodies such as stars, the galactic center, satellite galaxies of the Milky Way or Earth itself.

The only particles we are able to detect are stable ones, such as γ , e^+ , e^- , p , \bar{p} and ν . It is also possible to identify unstable particles through their decay products, such as the W boson decaying into leptons and neutrinos.

Neutrinos have the advantage that since they only interact weakly, they are mostly not scattered and go straight from the source to the observer. Experiments like IceCube [20] detect high energy neutrinos produced in the Sun. High energy gamma rays are also not scattered a lot, and dark matter annihilation can produce a monoenergetic gamma line which is furthermore dependent on the dark matter particle mass. Experiments such as the Fermi Gamma-ray Space Telescope [21] detect gamma rays. For charged particles, such as e^+ , e^- , p and \bar{p} , it is impossible to reconstruct the incoming direction since they are scattered multiple times before they arrive to the Earth. It is still possible to study their total flux. For example the PAMELA experiment [22] studies the total positron flux. For this kind of research, it is crucial to correctly model the astronomical background.

1.3.3 Direct detection

From astronomical observations, it was concluded that galaxies have a dark matter halo (see section 1.1.1). The particles making up dark matter halos only interact weakly and rarely scatter with baryonic matter. Direct detection experiments attempt to find those rare events.

Event rate

The De Broglie wavelength of a WIMP at a typical energy is $\lambda_{300\text{GeV}} \sim 5$ fm. Since it is comparable with the radius of a nucleus, such a WIMP scatters coherently with all protons and neutrons. The recoil energy of the nucleus (E_r) for a WIMP that hits a nucleus at rest is [3, Ch. 17]

$$E_r = \frac{|\vec{q}|^2}{2M_n} = \frac{2\mu^2 v^2 (1 - \cos\theta)}{2M_n} \quad (1.9)$$

where M_n is the mass of the nucleus, \vec{q} is the transferred momentum, θ the scattering angle and μ is the reduced mass

$$\frac{1}{\mu^2} = \frac{1}{m_\chi^2} + \frac{1}{M_n^2}$$

The velocity distribution of the dark matter particles v can be described by a Gaussian distribution [23] with mean $v = (220 \pm 20)$ km/s. For $m_\chi \ll M_n$ and $v = 220$ km/s, the recoil energy range between 1 and 200 keV, depending on the mass of the WIMP. This energy range must therefore be accessible in a direct detection experiment.

The differential event rate in a direct detection experiment is [3, Ch. 17]

$$\frac{dR}{dE_r} = N_N \frac{\rho_0}{m_\chi} \int_{v_{min}}^{v_{max}} \frac{d\sigma_{WN}}{dE_r} v f(v) dv dE_r \quad (1.10)$$

where $\frac{d\sigma_{WN}}{dE_r}$ is the differential cross section for the WIMP-nucleus scattering, N_N is the total number of target nuclei, ρ_0 [24] is the local WIMP density and depends on the halo model, and $f(v)$ is the velocity distribution of WIMPs. v_{max} is the escape velocity at the Sun distance from the center of the galaxy $v_{esc} = 544 \pm 50$ km/s. v_{min} is given by the minimum velocity that a WIMP must have to cause a recoil of energy E_r

$$v_{min} = \sqrt{\frac{E_r M_n}{2\mu^2}}$$

The total event rate is obtained by integrating the differential event rate over all the possible recoil energies, the minimum energy being the threshold of the detector.

To calculate the cross section of dark matter particles with SM particles, we distinguish the spin dependent and the spin independent cases. In the latter case, considering that a nucleus has Z protons and $(A - Z)$ neutrons, the total cross section is

$$\sigma \simeq \frac{4\mu^2}{\pi} [Zf_p + (A - Z)f_n]^2 \quad (1.11)$$

where f_p and f_n are the WIMP couplings to protons and neutrons, and can be written in analogy with neutrinos [3, Ch. 17]

$$f_{p,n} = \sum_{q=u,d,s} a_q f_{T_q}^{(p,n)} \frac{m_{p,n}}{m_q} + \frac{2}{27} f_{TG}^{(p,n)} \sum_{q=c,b,t} a_q \frac{m_{p,n}}{m_q} \quad (1.12)$$

where a_q is the strength of the coupling of a WIMP with a quark q . The term $f_{T_q}^{(p,n)}$ represents the contribution of the light quarks to the mass of the proton and the term $f_{TG}^{(p,n)}$ represents the interaction of the WIMP and the gluon density in the quark. The possible Feynmann diagrams are given in figure 1.8 and 1.9.

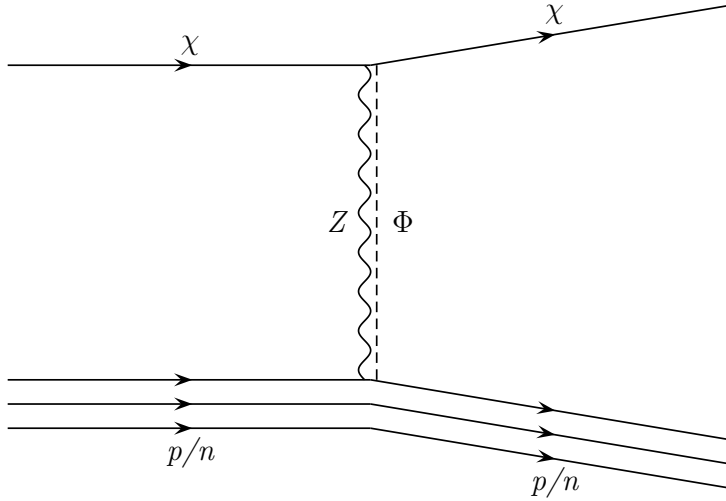


Figure 1.8

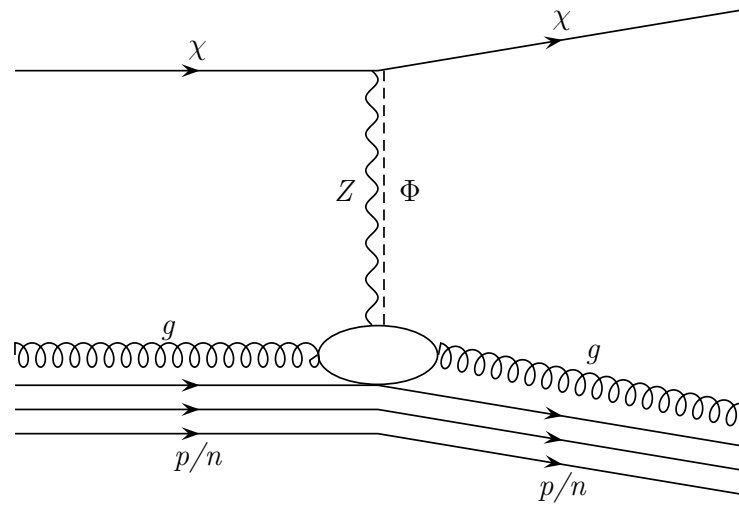


Figure 1.9

The spin dependent cross section has the same formula as equation 1.11 multiplied by an additional factor $J(J + 1)$, where J is the spin of the target nucleus. This cross section is always smaller than the spin independent cross section since in this case dark matter particles interact with nuclei with spin.

Direct detection techniques

Signatures for a the signal being due to a WIMP are:

- Nuclear recoils. Dedicated background studies are needed to reduce and model the background as much as possible.
- Annual modulation of the signal: since the relative velocity of Earth with respect to the Sun is not constant, there is a relative variation of the flux of dark matter particles with respect to the Earth. The flux variation generates a modulation of the event rate.
- Directionality: for the same reason as above, dark matter particles are incoming from different directions, depending on the time of the year.
- Energy distribution: the energy spectrum must fit the limits discussed in section 1.3.3.

When a WIMP scatters with a nucleus, it can generate three kind of signals:

- it can excite the nucleus, which then emits photons;
- the nucleus can emit charged particles such as electrons;
- the collision can produce vibrations of the target (phonons).

Different direct detection experiments look for one or more of this signals to detect nuclear recoils. Figure 1.10 shows some experiments with their sensitivity.

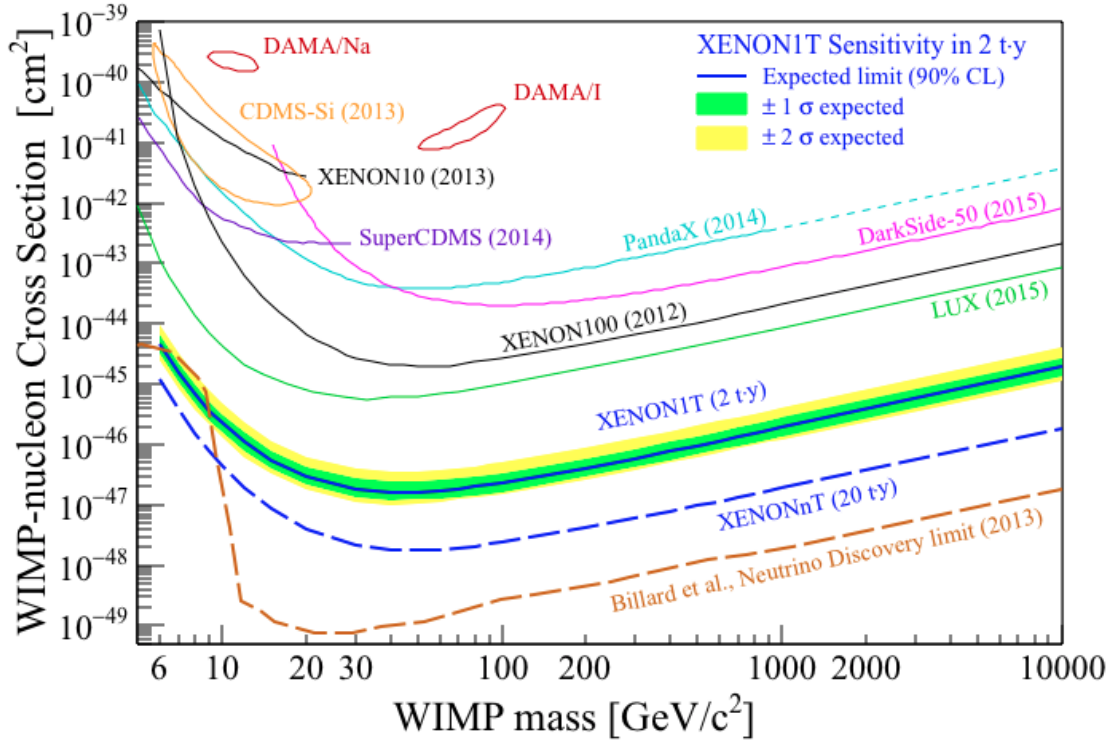


Figure 1.10: Exclusion limits and discovery contour of dark matter direct detection experiments. The expected sensitivity for XENON1T is also plotted: the solid blue line represents the mean value and the green and yellow band represents the 1σ and 2σ bands respectively. In light brown the neutrino discovery limit from [25] is plotted. Figure taken from [26]

The DAMA/LIBRA [27], CDMS [28] and SuperCDMS [29] experiments employ solid state cryogenic detectors. Energy deposition in the target material generate phonons that can be detected via temperature changes. In addition, it is possible to detect ionization (for example CDMS) or scintillation signals (for example DAMA/LIBRA).

The PandaX [30], DarkSide [31], LUX [32] and XENON1T [26] experiments employ liquid noble gases, argon or xenon. Both gases have good ionization and scintillation properties, which allow to measure the ionization and the scintillation signals (see section 2.1). In the next chapter, XENON1T will be described in details.

Chapter 2

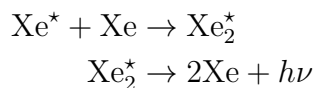
The XENON experiment

The XENON project employs liquid xenon (LXe) as a target for WIMP scattering, within a dual-phase time projection chamber (TPC). The first XENON experiment, XENON10, successfully set the first constraints for that time on the cross section of the WIMP-nuclei spin independent scattering [33]. The second experiment, XENON100, improved those limit by a factor of 10^3 [34] (see figure 1.10). Now the third experiment, XENON1T, is in commissioning.

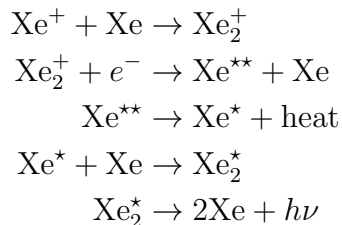
At the beginning of this chapter, a description of LXe as detection medium is given. Then the dual-phase TPC principle and the XENON1T experiment are described. In the last section, a detailed overview of the gas subsystems more relevant for this work is given.

2.1 Liquid xenon as scattering target

Liquid xenon as a scattering target offers many advantages. The energy deposition in LXe generates excited atoms (Xe^*) and ions (Xe^+) [35]. The excited atoms decay produces scintillation light with reaction



where $h\nu$ is the quantum of light output. The ions generates both electrons from the ionization process and scintillation light from the recombination reaction



Since background reduction is one of the most important task for direct dark matter detection (see section 2.3), xenon offers another important advantage. With the exception of ^{136}Xe , xenon has no long-lived radioactive isotopes. Additionally, liquid xenon's high density ($\sim 3\text{ g/cm}^3$) provides a strong stopping power. This feature is important to reduce the background.

Xenon has a molecular weight of 131.29 g/mol . Since the cross section (equation 1.11) is proportional to A^2 , using xenon as scattering target gives an higher event rate compared to neon and argon. However, at high energy recoil the form factor must be taken into account, which reduces the cross section (see figure 2.1). For more information on the properties of LXe see [35].

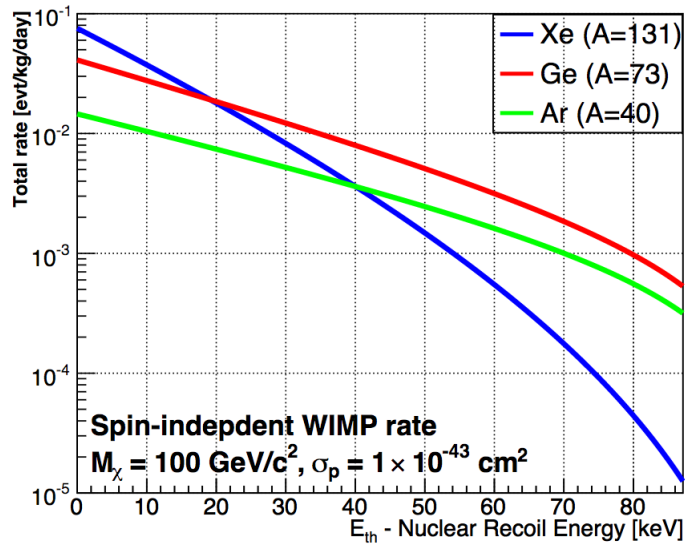


Figure 2.1: WIMP detection rate for three target materials, calculated for a WIMP mass of $100\text{ GeV}/c^2$ and WIMP-nucleon cross-section of 10^{-43} cm^2 . Figure taken from [36].

2.2 XENON detectors principle

2.2.1 Dual phase TPC and background discrimination

The XENON1T detector is a dual-phase (LXe and GXe) Time Projection Chamber (TPC) [26]. There are two arrays of photomultiplier tubes (PMTs), one at the bottom immersed in the liquid phase and one at the top, in the gas phase (see figure 2.2, left side). A scattering event in the LXe target generates scintillation light from the deexcitation and recombination chains and ionization electrons. The

prompt light signal is labelled S1 and it is detected by the PMTs at the top and at the bottom. At the same time, most of the ionization electrons are accelerated by an electric field towards the top of the TPC. At the liquid/gas interface, they are extracted into the gas phase by a strong field creating a secondary scintillation signal, labelled S2, which is proportional to the number of extracted electrons. The number of electrons that reach the liquid/gas interface N_e is equal to

$$N_e = N_e^0 \exp\left(-\frac{t_d}{\tau_e}\right) \quad (2.1)$$

where N_e^0 is the number of electrons generated at the beginning, t_d is the time required for the electrons to drift to the liquid/gas interface and τ_e is the electron life-time inside the detector.

S2 is delayed with respect to S1 by t_d , allowing to reconstruct the vertical position of the scattering event (figure 2.2, left side). It is important to have a large τ_e to detect low energy events and events at the bottom of the TPC. Additionally, the position on the horizontal plane is reconstructed from the distribution of the light collection on the top array, allowing to determine the 3d vertex of the interaction.

The 3d position reconstruction allows to apply a cut on the position. As already stated in section 2.1, xenon has a high stopping power, so most of the background events are expected to happen at the border of the detector. A fiducial cut volume is applied (see figure 2.3).

In addition, it is possible to discriminate between nuclear and electronic recoils using the ratio S2/S1. An electronic recoil event is due to γ and β particles, which are part of the background. WIMP particles generate only nuclear recoil events. The light yield in the two events is different (figure 2.2, right side), allowing to cut the electronic background. Figure 2.4 shows XENON100 calibration using a gamma source (blue dots) and a $^{241}\text{AmBe}$ neutron source (red dots). In XENON100 this technique has successfully been employed to reject 99.75% of electronic recoil [34]. A leakage is still present from the electronic band to the nuclear band, so the electronic background must be studied.

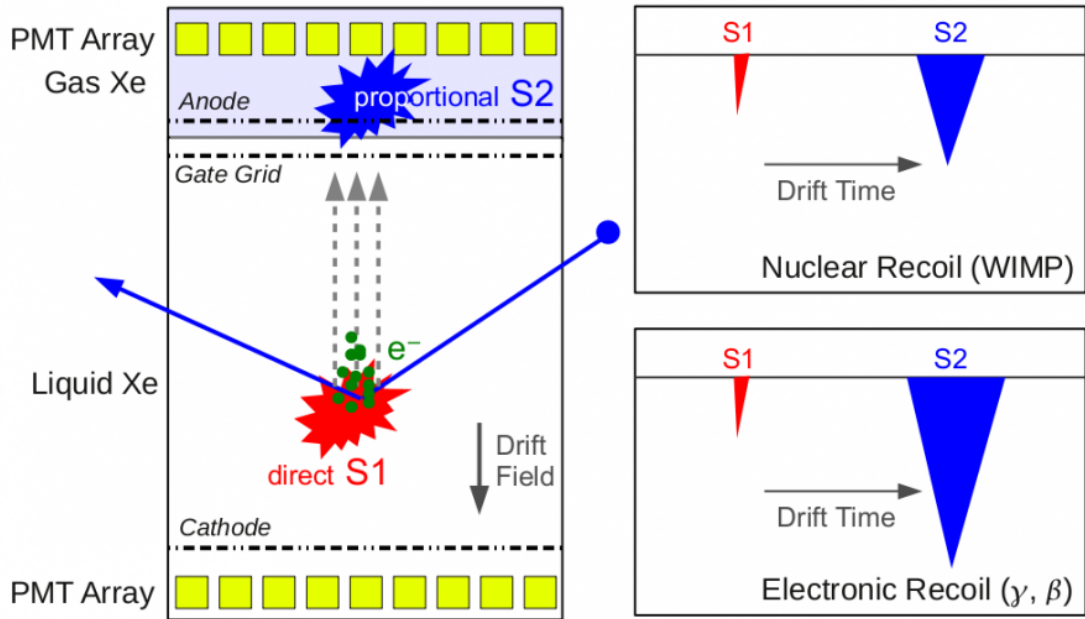


Figure 2.2: (Left) The XENON detection principle with a two-phase time projection chamber. (Right) Sketch of two events, electronic and nuclear recoil. Figure taken from [37].

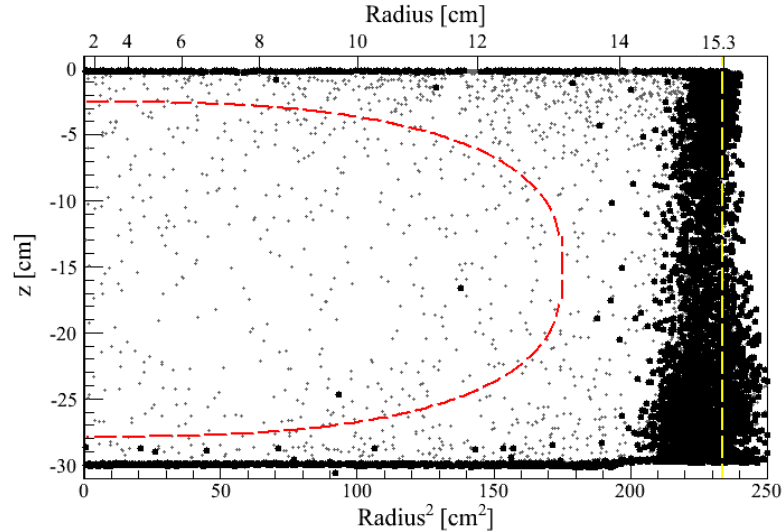


Figure 2.3: Spatial distribution of the electronic and nuclear recoil events inside the active LXe volume in the XENON100 experiment, in the (6.6 – 43.3) reconstructed energy range. The dashed red line indicates the fiducial volume. Figure taken from [34].

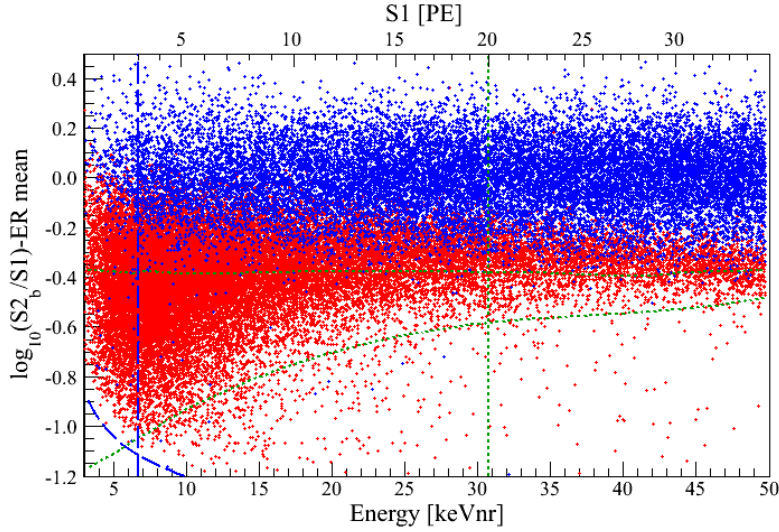


Figure 2.4: Event distribution in the discrimination parameter space $\log_{10}(S2/S1)$ as a function of the reconstructed deposited energy (keVnr). The blue dots indicate an electronic recoil while the red dots indicate a nuclear recoil. The dashed lines indicate the cuts used in early XENON100 analysis, while later a maximum likelihood approach is used [38]. Plot from the XENON collaboration, data from [39].

2.2.2 XENON1T detector design

XENON1T has a total inventory of 3.3 tonnes of LXe [26]. The LXe is contained in a double wall cryostat made of 5 mm thick low radioactive steel. The outer cryostat is large enough to be employed for the next generation XENON experiment, XENONNT. The fiducial volume is about 2 tonnes of LXe and is viewed by the two PMT arrays. The top array has 127 PMTs arranged in concentric rings to better localize the interaction on the perpendicular plane. The bottom array has 121 PMTs arranged in an exagonal structure to maximize the light collection.

The electric field in the TPC is generated through electrodes made of stainless steel meshes or copper wires around stainless steel rings. The PMT arrays are screened from the electric field using ground meshes positioned right above or below the array (for the bottom and the top array respectively). The cathode is positioned at the bottom of the TPC. At the gas/liquid interface there are two electrodes: a gate grid just below the liquid and the anode above, creating the amplification region. To ensure the uniformity of the electric field, a stack of 74 field shaping rings is placed on the border of the inner vessel.

The cryostat is placed in the center of a 9.6 m diameter water tank used both as shield and as active Cherenkov muon veto with 4π coverage [40]. Every event

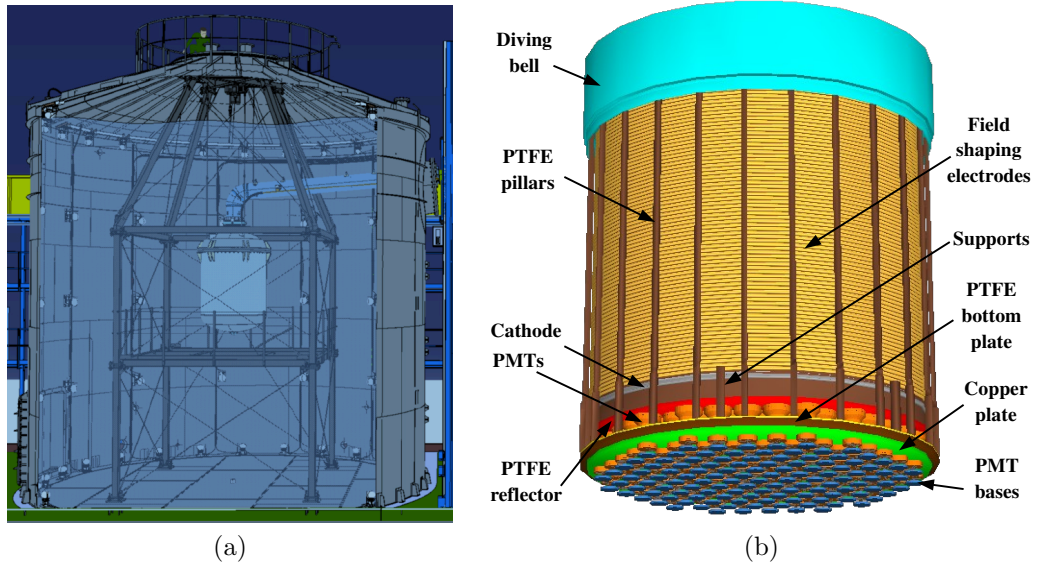


Figure 2.5: Rendering of the cryostat and water tank. Figure taken from [26].

that has a coincidence in the muon veto can be discarded to reduce background.

2.3 Background of XENON1T

One of the most important task in dark matter direct detection is the reduction and discrimination of background. WIMP-nucleus scattering is a rare event, thus it is necessary to model and quantify all possible sources of background. While it is possible to discriminate electromagnetic recoils using ionization vs scintillation light, neutrons produce a signature that is indistinguishable from a WIMP event and must be reduced as much as possible. The background sources can be divided in two categories: external and internal.

2.3.1 External background

All sources of background that are outside of the detection medium are called external background. The most notable source is the cosmic radiation, but it also includes natural radioactivity from the environment and from the materials used to build the detector.

Cosmic radiation flux includes all kinds of particles at many different energies. In particular, muons have a large penetration depth and can produce neutrons via electromagnetic showers, spallation or secondary processes. To shield the experiment from cosmic radiation, XENON1T is hosted at the *Laboratori Nazionali*

del Gran Sasso (LNGS), in L'Aquila, Italy¹. The LNGS underground facilities have an average of ~ 1400 m rock above (or 3700 m water equivalent), reducing the atmospheric muon flux by about 6 orders of magnitude. Figure 2.6 shows a comparison of the muon flux for different underground facilities.

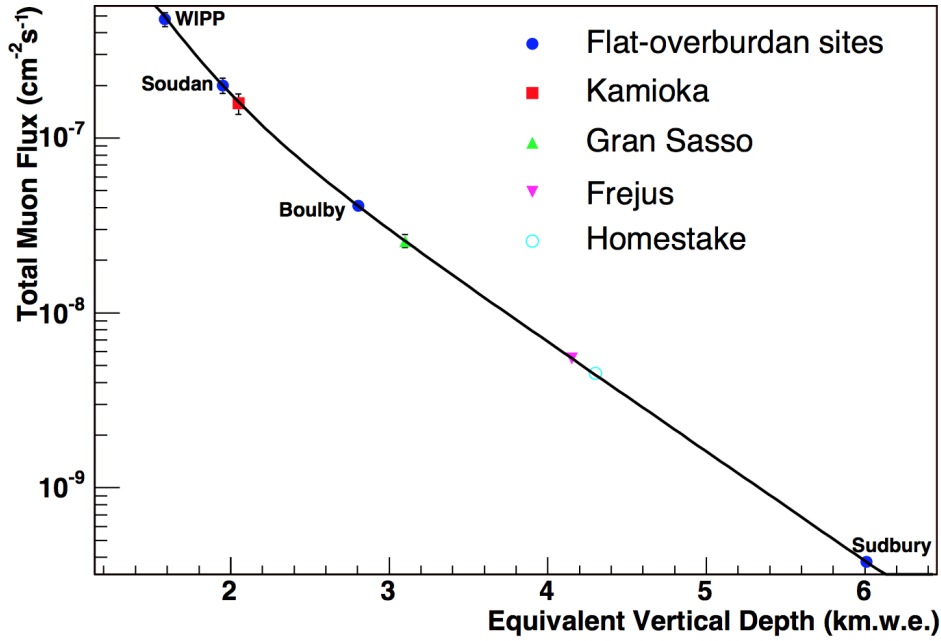


Figure 2.6: Total muon flux measured for the various underground sites as function of the equivalent vertical depth relative to flat overburden. Figure taken from [41].

Even if the detector is shielded against cosmic rays, natural radioactivity still contributes to the background. Some elements, such as $^{238-235}\text{U}$, ^{228}Th , ^{40}K , have radioactive decay chains which produce several α , β and γ particles. Neutrons are produced in (α, n) reactions and spontaneous fission. The water tank shields from neutrons coming from the environment, but it is also necessary a preliminary screening of the materials to avoid any radioactive contamination.

2.3.2 Internal background

Internal background sources are within the detection medium itself. As already explained in section 2.1, one of the advantages of xenon is that it is a stable element. The largest contribution to the internal background comes from contamination of the xenon with the radioactive noble gases krypton and radon [26].

¹www.lngs.infn.it/

Radon Radon is the heaviest noble gas and has no stable isotopes. ^{222}Rn is produced in the decay chain of ^{238}U , which can be present at trace level within the materials used to build the detector. ^{222}Rn has a lifetime of 3.8 days and, once is created, can easily diffuse inside the fiducial volume since xenon and radon have similar chemical properties. One of the product of the ^{222}Rn is ^{214}Pb , which decays emitting β radiation and is a dangerous background source. To quantify this background, an accurate estimate of the radon emanating from the whole system has been done.

Krypton Xenon is commercially produced by extraction from air. The natural abundance of xenon in air is 0.09 part per million by volume (ppm) [42]. Krypton is produce along with xenon and has a natural abundance of 1.14 ppm, a factor of 10 higher than xenon. Xenon and krypton are separated by distillation, but the limited efficiency causes traces of krypton in commercially available xenon of part per million (ppm) to part per billion (ppb). Natural krypton has no radioactive isotopes, but ^{85}Kr , byproduct of nuclear fission, is a β^- emitter with $T_{1/2} = 10.8$ yr. The goal for XENON1T is to have less than 2 ppt of natural krypton in the xenon inventory [26]. To achieve this concentration, a distillation column is used to distill the xenon inventory.

2.4 Subsystems

The XENON1T gas system contains several subsystems necessary for the regular operations. Figure 2.9 shows a schematic of XENON1T gas system. There are four subsystems:

- Cryogenic system (green);
- Purification system (red);
- ReStoX (blue);
- Bottle rack (yellow).

In this section, there is a short description of the first two and a more detailed one of the last two.

Cryogenic system. It comprises the cryostat, with the TPC, and the cooling system. There is a heat exchanger and three Pulse Tube Refrigerators (PTRs), two for normal operations and one for emergency cases.

Purification system. The purification system provides a continuous purification of xenon during normal detector operations. The xenon is taken from the cryostat, passes through two high temperature gas purifiers and is brought back to the cryostat. Furthermore this system connects all subsystems and the distillation column to each other and is therefore used as a distributor.

2.4.1 ReStoX

The Recovery and Storage of Xenon system (ReStoX) is a large spherical pressure vessel. It is used to:

- store xenon transferred from individual bottles;
- store purified xenon from the distillation column;
- liquefy gaseous xenon;
- fill xenon into the detector;
- recover xenon from the detector.

ReStoX has a capacity of 7.6 tonnes of xenon [43]. The xenon inventory of XENON1T is comprised of 3.3 tonnes, but ReStoX can also be used for XENONNT, the next generation XENON experiment. The system can operate at any pressure from vacuum up to 72 bars, and at a temperature range from -196°C to room temperature. The xenon can be stored in solid, liquid, gaseous or supercritical phase.

ReStoX is composed of two concentric stainless steel spheres, with minimal thermal contact. The diameter of the inner sphere is 2124 mm and the diameter of the outer sphere is 2400 mm. The inner sphere stores the xenon, while the outer sphere provides thermal insulation. The space between the two spheres is evacuated for maximum insulation and contains the liquid nitrogen pipe system that cools the inner sphere.

There are many ports that connect ReStoX to the purification system and the main detector. To fill xenon from ReStoX to the detector, liquid xenon is taken from the bottom of ReStoX and goes through a heat exchanger, which



Figure 2.7: Picture of ReStoX.

evaporates it. Afterwards, the xenon is purified, liquified again through the same heat exchanger and filled into the detector. However, to fill xenon inside ReStoX, a port that sits on top of the sphere is used.

2.4.2 Xenon Bottle Rack

The bottle rack provides an interface to connect the xenon bottles that contain the xenon inventory to be emptied with the XENON1T gas system. It is used for:

- xenon analysis;
- bottle to ReStoX filling;
- bottle to main detector filling;
- bottle to bottle distillation;
- recuperation from ReStoX to bottle;
- recuperation from main detector to bottle;

The bottle rack has three main parts: the filling side, the recuperation side (both in figure 2.8a) and the analytics side (figure 2.8b). For a detailed scheme of the bottle rack, see figure 2.8c.

The filling side of the bottle rack is composed of a long tube that connects the recuperation and the analytics sides. Four spiral shaped pipes are connected on this tube, referred in this work as “pipettes”. They are located at regular intervals on the length of the tube. On each one of them it is possible to connect a xenon bottle. In figure 2.8c, the pipettes are between the valves FV1201 and FV1202, FV1203 and FV1204, FV1205 and FV1206, FV1207 and FV1208. The bottles are standing on scales to measure their weight. Since xenon is critical at room temperature, it is impossible to monitor the amount of xenon in one bottle only by the pressure.

The spiral shape of the pipettes has many advantages: it is easier to connect bottles of different height and it allows to reduce the influence of the bottle connection on the weight measurement. The spiral design allows a longer pipe, which results in a larger xenon sample. When exchanging a bottle, only the spiral pipes are exposed to air which reduces the pumping time needed to get rid of it.

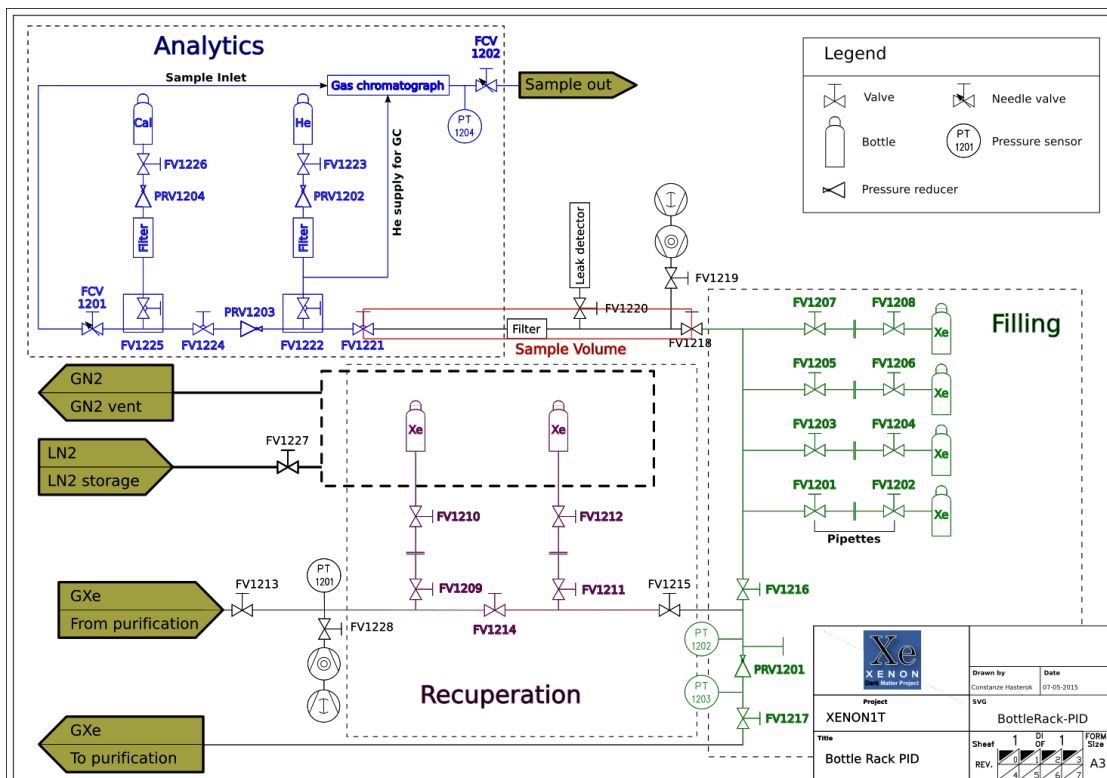
The recuperation side provides an easy interface to connect up to two bottles and submerge them individually in liquid nitrogen. The recuperation of xenon is done by cryogenic pumping. The dewar used for the liquid nitrogen is visible in the center of figure 2.8b. Each bottle is hooked up to a dynamometer to monitor their weight.



(a) Filling and recuperation side. On the right there are the 4 filling bottles and on the left the 2 recuperation bottles.



(b) Analytics side. The brown bottle on the right is Helium and the green one is calibration gas.



(c) Schematics of the bottle rack. The valves the valves next to each bottle are the valves of that bottle.

Figure 2.8: Pictures and schematics of the bottle rack.

The analytics side is used to analyze the xenon with the technique of gas chromatography (see chapter 3). It was mostly used to analyze the xenon from the bottles before emptying them into ReStoX, but it can also be used for the gas in ReStoX. It comprises a sample volume to store xenon for the measurements (between valve FV1218 and FV1221), the gas chromatograph used for the measurements (explained in detail in section 3.2.2) and the gases needed to run the gas chromatograph. With samples from four bottles, the xenon in the sample volume has a pressure of ~ 20 bar. The pressure reducer PRV1203 reduces the pressure to 1.2 bar, the pressure needed for the measurement with the gas chromatograph, and a particle filter (not shown in figure 2.8) prevent harmful particles from reaching the gas chromatograph.

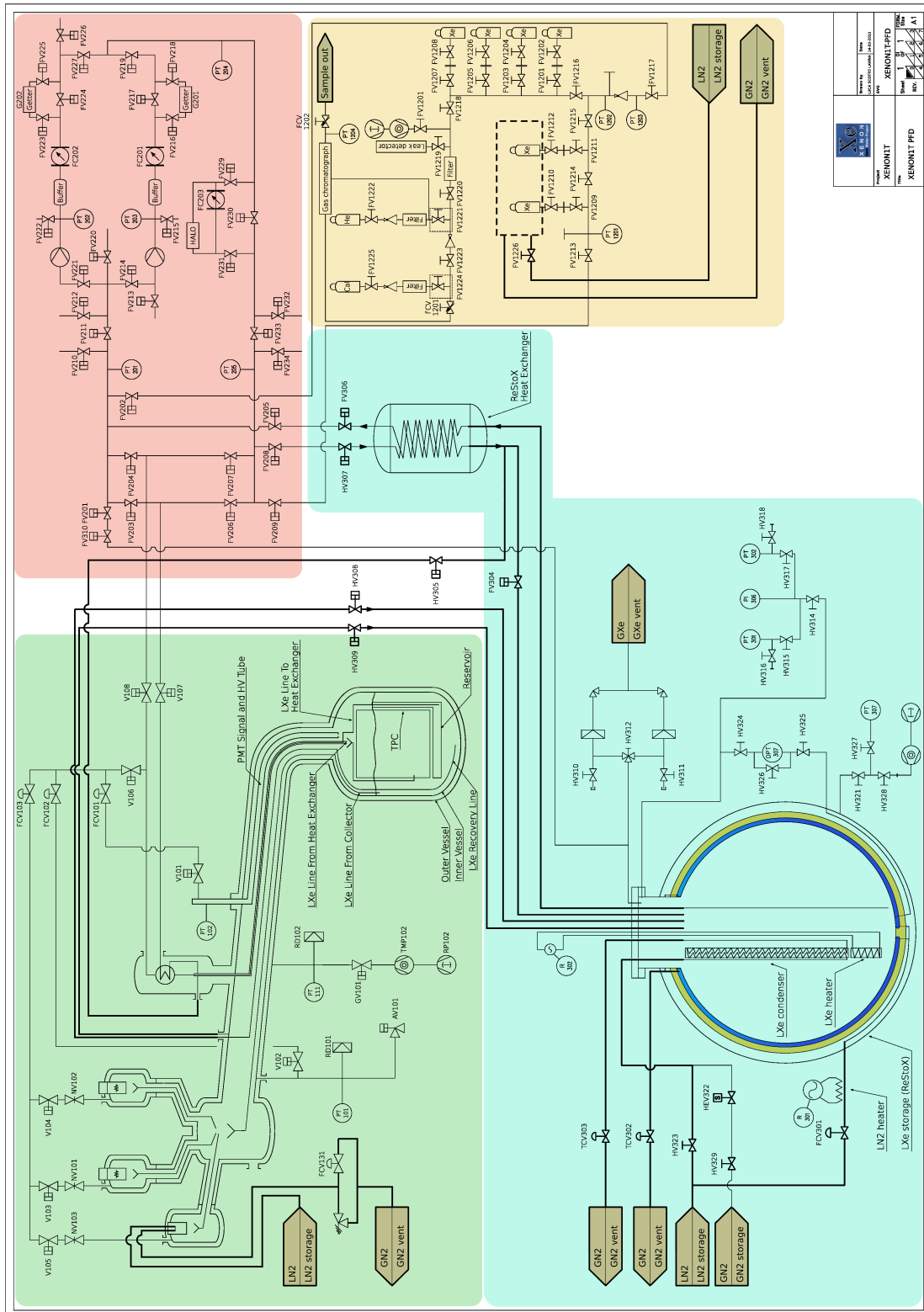


Figure 2.9: Schematics of XENON1T gas system.

Chapter 3

Gas purity measurement of xenon

To achieve the target sensitivity in dark matter searches with XENON1T, only very pure liquid xenon must be filled to the detector. For this reason, measuring the impurities contained in the xenon bottles prior to filling them into ReStoX is essential. Around 150 bottles have been filled to ReStoX to reach the 3.3 tonnes required. Up to 4 bottles at one time have been measured, given that they were provided by the same company and had the same certificate.

In this chapter, a setup to measure a small sample of xenon from each bottle using gas chromatography is presented. First, a general introduction on gas chromatography is given. Then the experimental setup of the gas chromatograph at the bottle rack is explained in details. The development and the optimization of the setup was beyond the scope of this work and it is described in [44]. In section 3.5 some of the results of the bottles measured during this work are presented. Finally, the results of the whole inventory are given and some effects that occurred during the measurements are outlined.

3.1 Motivation

As explained in chapter 2, there are two types of dangerous impurities for a liquid noble gas detector. The first type is radioactive impurities (see section 2.3.2). In particular, it is necessary to monitor the krypton concentration of each bottle before filling. The xenon inventory is distilled before the start of the experiment, but a higher krypton concentration leads to a longer distillation time and a higher xenon loss due to off-gas. For this reason, it is important to identify the bottles with a too high concentration of krypton and distill them separately.

The second type are the electronegative impurities. Electronegative molecules, such as O_2 and H_2O , trap electrons. This reduces the electron life-time τ_e in the detector. As explained in section 2.2.1, it is important to have a large τ_e to detect

low energetic events or events that happen at the bottom of the TPC. For this reason those impurities should be as low as possible. In addition to distillation, high temperature gas purifiers can be used to remove this type of impurities.

With gas chromatography, it is possible to measure hydrogen, oxygen, nitrogen, argon, methane, krypton and carbon oxide. Radon can not be measured. N_2 serves as tracer for air where the impurities of interest, Kr and O_2 , have concentration 1.14 ppm and 21% respectively [42].

If concentration of impurities in one bottle is less than the required amount (< 50 ppb of Kr and < 30 ppm of O_2 and N_2), the bottle is filled directly into ReStoX. The bottles that have an higher concentration have been distilled separately before being filled.

3.2 Gas chromatography

3.2.1 Introduction to gas chromatography

Chromatography is a widely used separation technique to analyze the components in a mixture [45]. Chromatography can be used with gaseous and liquid samples. Chromatography employs two phases to separate the elements: a stationary phase with a large surface and a mobile phase. The elements of the sample are separated based on their partial pressure if they are gaseous and their affinity with the stationary phase.

For gas chromatography, the mobile phase is a gas, called carrier gas, and the stationary phase can be liquid or solid. Some example of carrier gases are hydrogen, helium or nitrogen. The system has to be leak tight in order to avoid contamination, so the stationary phase is placed inside a leak tight pipe called column. For our setup, the carrier gas is helium, and the stationary phase is solid. Helium has no adsorption effects and elutes at maximum velocity from the column. The other gases travels slower through the column and have slower retention time, different for each impurity. Gases like H and N_2 have small interaction with the adsorbent phase, so their retention time is fast. Polar molecules like H_2O interact strongly with the stationary phase and have long retention times. Big elements such as Xe are also slow because their radius has the same order of magnitude of the pores of materials inside the column.

To detect the elements at the outlet of the column, a pulse discharge detector (PDD) is employed. The working principle of a PDD is the ionization of the gases with high energy photons [46]. The photons are generated by a high voltage discharge between two platinum electrodes in pure helium gas. The photons emitted have energy range from 13.5 eV to 17.5 eV, enough to ionize all elements but helium and neon. The resulting current is measured on a collector electrode

and constitutes the signal. The response of the PDD is linear over 5 order of magnitudes and allows a ppm level calibration gas for ppb level signal. The signal is plotted over time to individuate the retention time of the ions peaks. This is called chromatogram.

3.2.2 Experimental setup

A gas chromatograph of type Trace GC Ultra from Thermo Fischer is used for the analysis. It was customized and optimized for the measurement of impurities in xenon during a doctoral thesis at MPIK [47, 44]. Figure 3.1 shows the picture of the chromatograph and the data acquisition computer at LNGS. Figure 3.2 shows a scheme of the inner setup.



Figure 3.1: Picture of the commercial gas chromatograph and the DAQ computer.

There are 3 columns in the setup: the column called “sample circuit” in figure 3.2 is not filled with adsorbent and has the function to store the sample. Its volume is about 20 ml. The “pre-separation” column, filled with HayeSep¹, has the function to separate gases with big retention time from ones with small retention time. The “fine column” on the right of figure 3.2 has finer pores compared to the previous column and it is used for the final separation of the elements before the PDD. It uses a molecular sieve with 5 Å diameter pores. The fine column is placed in a cryo-oven, used to increase the temperature, which decreases the retention time.

¹www.vici.com/hayesep/hayesep.php

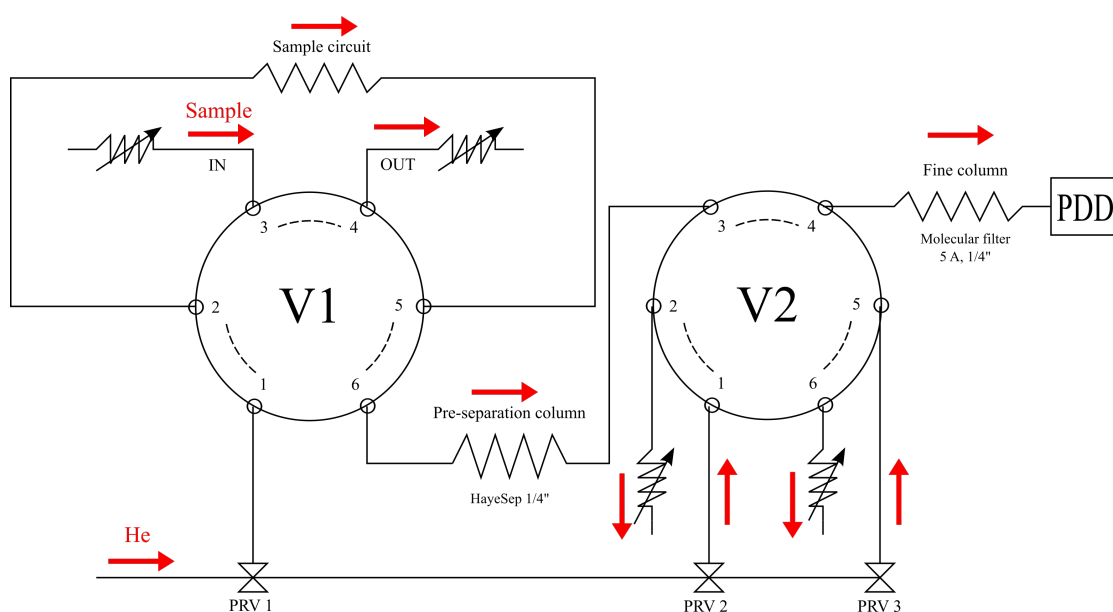


Figure 3.2: Valve setup of the gas chromatograph. PRV1, PRV2, and PRV3 are pressure reducers. The jagged lines are the columns and the jagged lines with arrows indicate the adjustable flow resistances. All the columns have 1/4 inch section and the lines between the columns and the valves have 1/8 inch section. The red arrows indicate the gas flow.

There are two reasons to have a pre-separation column to separate xenon: first xenon is heavy and has a high adsorption rate, so it takes several hours until it eluted from the fine column (while krypton, for example, only has 20 minutes retention time). Second, the gas chromatograph is set up to measure gas concentrations at ppb level, while xenon is the main component of the gas sample: the amount of xenon in the sample would saturate the PDD. Xenon can be prevented from reaching the fine column by valve switching. The corresponding method will be described below.

Two diaphragm MDVG valves from Analytical Flow Products are used for the measurements. Each valve, denoted as V1 and V2 in figure 3.2, has 6 ports, connected in pairs. When the valve is switched off, the inlet pair with no dashed lines are connected. When switched on, the pairs the dashed lines are connected.

Measurement method

The Trace GC Ultra software provides automatic data collection. The software is used to program a method that saves the data while switching valves and changing the temperature of the cryo-oven. One method, summarized in table 3.1, has been used for all the samples: background, calibration and xenon. Before the start of the measurement, both V1 and V2 are switched off. The initial temperature of the cryo-oven is 60°C. The sample is flushed in through port 3 of V1, goes through the sample circuit and is flushed out through port 4 of V1. The carrier gas goes from port 1 to port 6, passes through the pre-separation column, and it is flushed out from port 2 of V2. The PDD is constantly flushed by the helium going through port 5 and 4. It is important to have a flow as constant as possible in the PDD to have a stable baseline.

At the beginning of each measurement, V2 switches on, so that the gas from the pre-separation column goes through the molecular filter and then to the PDD (segment one of figure 3.3). The switching on and off of valves causes a change of flux in the PDD and hence changes the baseline (visible in figure 3.3). Furthermore, the valves are not perfectly leak tight and a small amount of air is introduced in the system each time they switch. The baseline changes with some delay since the gas has to go through the columns. A waiting time of around 10 minutes is necessary before the injection of the sample in order to wait for those impurities to leave the system.

Once the baseline is stable, V1 switches on and the gas stored in the sample circuit is pushed by the helium into the pre-separation column (segment 2). There, components with low retention time are separated from the xenon. To avoid xenon to reach the PDD, V2 is switched off after additional 6 minutes (segment 3): this way, the gas from the pre-separation column is flushed out through port 2 of V2 and the remaining sample is pushed by the helium from port 5 of V2. The 6

minutes time was optimized such that most of the components have already left the pre-separation column but xenon hasn't reached the fine column yet.

The gas components reach the detector in the following order: hydrogen, oxygen and argon, nitrogen, krypton, methane and carbon monoxide. Oxygen and argon have the same exit time and it is impossible to distinguish them. After 30 minutes from the start of the measurement, the temperature of the main oven is increased up to 100°C in order to speed up the exit of slower elements such as CO and H₂O (segment 4). The increase in temperature causes an increase in the baseline and, if present, impurities to elute from the column.

Segment	V1	V2	Cryo-oven temperature (°C)
1	off	on	60
2	on	on	60
3	off	off	60
4	off	off	100

Table 3.1: Setting for the measurement method of the gas chromatographs in the time segments of figure 3.3.

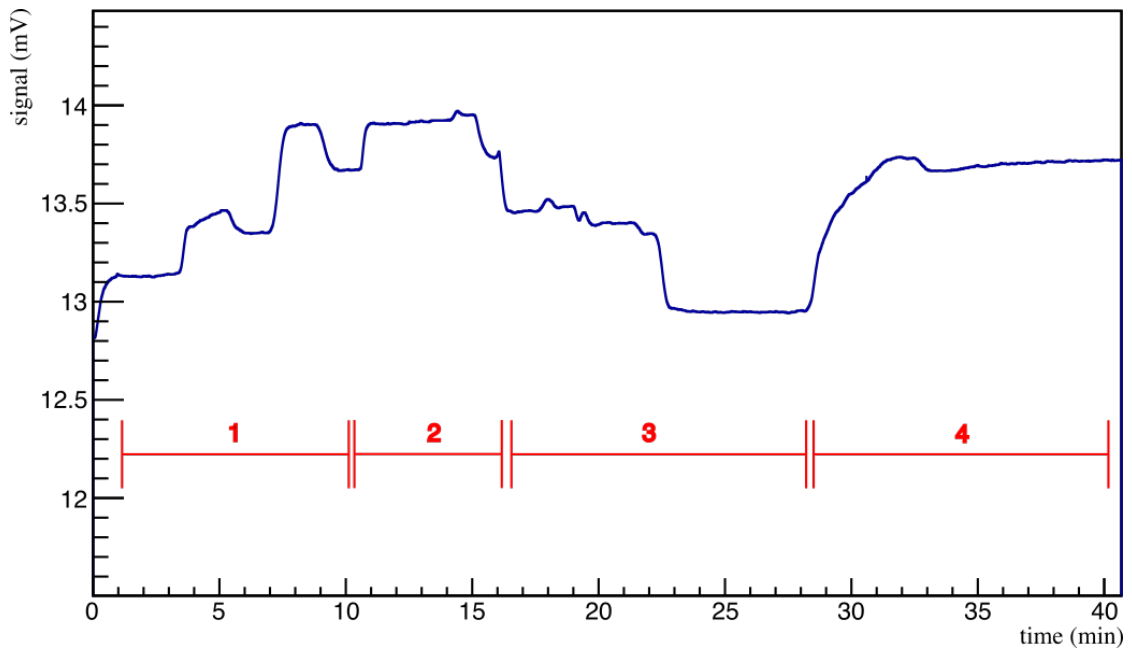


Figure 3.3: Background chromatogram.

3.2.3 Calibration gas

To calibrate the gas chromatograph, a custom calibration gas mixture based on helium is used. The impurities are present at ppm level, which is roughly the same order of magnitude of the impurities expected in the xenon samples. CO₂ and Xe are also present in the calibration gas, but are not visible in the calibration chromatogram since the method rejects them before they reach the PDD.

Impurity	Concentration (ppm)	Uncertainty (ppm)
H ₂	4.97	0.15
O ₂ + Ar	17.06	0.45
N ₂	12.6	1.3
Kr	11.10	0.22
CH ₄	5.16	0.10
CO	5.17	0.10
CO ₂	9.88	0.20
Xe	5.05	0.10

Table 3.2: Amount of impurities in the calibration gas used in this work.

3.3 Procedure

3.3.1 Background and Calibration

Before taking xenon data, it is necessary to have a background and calibration measurement, to check the stability of the gas chromatograph. The PDD baseline has a slow decreasing trend on a timescale of days, which is due to the countinuous helium flushing that cleans the columns, and it is necessary to monitor it since it impacts the sensitivity. Moreover, background chromatograms show if there are unexpected peaks due to the internal background or other shapes in the baseline, usually due to xenon or other particles that are stuck in the columns.

Background Measurement The sample loop is flushed with the carrier gas, helium 6.0² that is further cleaned with a high temperature gas purifier. In this chromatogram, only the baseline changes due to the valves switching and internal background are visible.

²6.0 means that the concentration of the total amount of impurities inside the helium is less than 10⁻⁶%.

Calibration Measurement A calibration is performed at least once per day to monitor the detector response to each gas. The sample loop is flushed and filled with calibration gas.

3.3.2 Xenon

Even if the data acquisition method is automatic, the operations at the bottle rack are manually performed. After connecting the four xenon bottles to be filled, the recuperation and analytics side of the bottle rack are pumped and baked until a pressure of $\sim 10^{-7}$ mbar. Once the pressure is low enough, all the valves on the filling side and FV1221 are closed (see figure 2.8c). The valves of the xenon bottles (FV1202, FV1204, FV1206 and FV1208) are then opened and closed after some seconds to store a sample of xenon in the pipettes. The bottle valves will not be opened again until they are emptied in ReStoX.

All the pipettes have the same volume. Assuming that the bottle pressure is the same for all the bottles the amount of gas taken from each bottle is the same. Bottles where the pressure was known to be different have been measured individually.

After storing the xenon in the pipettes, the valves FV1201, FV1202, FV1203 and FV1204 are opened. In order to achieve a better mixing of the gas in the pipe connecting the pipettes, the valves are opened and closed in small steps one after the other. Once all the xenon from the pipettes is expanded in the pipe, valve FV1218 is opened to let the xenon expand in the sample volume. Valve FV1218 is then closed and stays closed for the rest of the measurement. The xenon left in the volume between valve FV1218 and valve FV1216 and in the spirals is later filled into ReStoX too. Note that the whole procedure takes less than 10 minutes. This will be important for the second part of this work where we will study the gas mixing properties of xenon.

The pressure inside the sample volume is usually ~ 20 bar, enough to make 3 measurements. A xenon measurement is repeated twice in order to check the reproducibility. Once the xenon is stored, the helium flow in the sample inlet is interrupted (closing valve FV1222) and valve FV1218 is opened to let the xenon flush through the sample circuit. The pressure reducer PRV1203 lowers the xenon pressure to a small overpressure, to have a continuous flow of xenon in the sample circuit.

In order to have comparable measurements, it is necessary to have the same amount of gas in the sample loop. To ensure this, the flow and the outlet pressure of the xenon in the sample circuit are regulated by using the needle valves FCV1201 and FCV1202.

In order to minimize the amount of xenon required for one measurement, FV1221 is closed when V1 switches on. Once the xenon between FV1221 and

FCV1201 is finished, FV1222 is opened to have helium flow again in the sample circuit, in order to prevent air from drifting inside the sample loop. After each measurement, the fine column is baked at 100°C and flushed with helium to purge gas components with longer retention time.

3.4 Analysis

The identification and evaluation of the impurities in xenon is done comparing the area of each peak of the calibration gas with the area of the peak at the same time (if present) in the xenon sample. The impurities have the same retention time, independently if they are in xenon or in helium. In this analysis, it is assumed that the response of the PDD to a certain impurity is linear with its abundance and the separation efficiency of impurities from xenon is 100%. It is also assumed that the background chromatogram is the same for xenon and calibration gas.

To evaluate the area of one peak, first a gaussian fit is performed in the calibration chromatogram. A peak region for each impurity is isolated, considering the 4 sigma region of the gaussian fit. For carbon monoxide, since it does not have a gaussian shape, instead of a gaussian fit a 5 minute interval is taken. With the exception of O₂ and Ar, the peak regions of different impurities do not overlay with each other.

The area of the peaks of calibration and xenon chromatograms is calculated by integrating in the peak region. Since the height of the baseline changes from measurement to measurement, a linear fit is performed in the region between 6 and 4 sigma, excluding the peak region, where the baseline is mostly flat. The line function is integrated in the signal region and its integral is subtracted from the total peak area.

For the background chromatograms, the same procedure has been applied. If the baseline was flat, the evaluated area would be close to 0 since the fluctuation would average out. Because of the features in the baseline, this area is greater than 0. The background area is subtracted from the peak area of calibration and xenon chromatograms of the same day to take into account this effect.

The formula used to calculate the concentration of each impurity (Q) in xenon is

$$Q_{Xe} = Q_{cal} \frac{(A_{Xe} - A_{bkg})}{(A_{cal} - A_{bkg})} \quad (3.1)$$

where A_{Xe} , A_{cal} , A_{bkg} are the area of the peak of each impurity in xenon, calibration and background chromatograms respectively.

The dominant errors of the concentration are the uncertainty of the concentration of the impurities in the calibration gas Q_{cal} (see table 3.2) and the systematic

uncertainty coming from the method with which the peak areas have been calculated.

3.5 Results

In figure 3.4 one background, one calibration and one xenon chromatogram are overlaid. The xenon sample was taken from bottles APE856030H, 10092191, 8984026 and 8673499. The sample was measured twice but only one measurement is shown in figure.

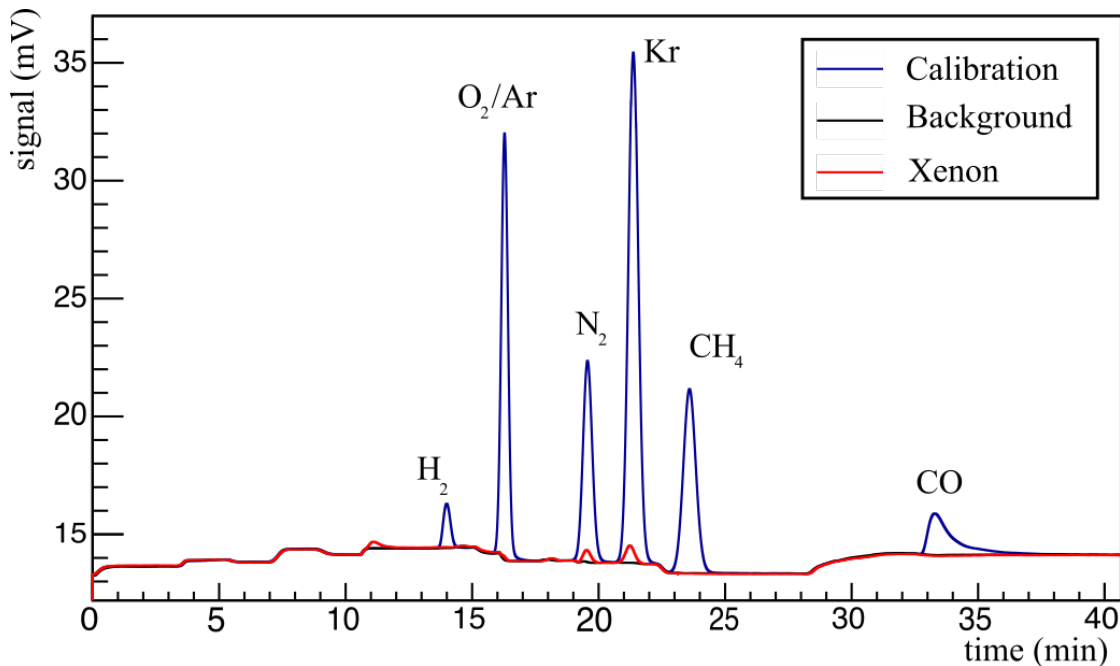


Figure 3.4: Background, calibration and xenon chromatograms. All the measurements have been taken the same day.

Table 3.3 lists the measured impurity concentrations of the xenon sample. The two measurements are in agreement within errors and all the values are lower than the ones provided by the certificates.

The gas chromatograph setup is sensitive enough to measure the interesting impurities, O₂ and Kr. All the measured concentrations are consistent with the certificate provided by the company. The measured bottles can be filled into ReStoX since they meet the requirements given in section 3.1. It is worth noting that not all the bottles were pure as expected from the certificate (see section 3.5.2). Most of the times, this was due to the fact that the xenon bottles have been used previously at other experiments.

Impurity	Meas nr 1 (ppm)	Meas nr 2 (ppm)	Certificate (ppm)
H ₂	< 0.06	< 0.06	/
O ₂ + Ar	< 0.06	< 0.06	< 1.2
N ₂	0.64 ± 0.06	0.52 ± 0.11	< 1.8
Kr	0.36 ± 0.03	0.39 ± 0.02	0.40 ± 0.4
CH ₄	< 0.03	< 0.03	< 0.2
CO	< 0.3	< 0.3	/
H ₂ O	/	/	< 1

Table 3.3: Measurements of the bottles number APE856030H, 10092191, 8984026 and 8673499, provided by Areogas. The certificates don't provide any number for H₂ and CO. The gas chromatograph is not sensitive to water.

3.5.1 Total amount of impurities

From the individual measurements of all the xenon bottles, it is possible to calculate the expected amount of impurities in the whole xenon inventory of 3.3 tonnes. For this calculations, the different amount of xenon stored in the bottles, and the mixing of samples from several bottles have been taken into account.

As a cross check at the end of the filling campaign, a measurement of the ReStoX gas phase has been done. The xenon has been extracted using the same pipe used to transfer gas from the bottles to ReStoX. This pipe is located at the top of ReStoX. The ReStoX pressure was increased up to 2.1 bar in order to have a sufficient overpressure to ensure a continuous gas flow from ReStoX to the analytics part of the bottle rack.

A sample from ReStoX gas phase was drawn on two different days. The measurements of the sample on the first day showed a high contamination of hydrogen. Table 3.4 lists the hydrogen concentrations for the four consecutive measurements of the sample. A strong decreasing trend is clearly visible. One possible explanation is the accumulation of hydrogen in the pipes from outgassing during the weeks they were not used. On the second day a sample was drawn after flushing the pipes with xenon from ReStoX. The xenon used for flushing was stored in a recuperation bottle.

Measurement nr.	Hydrogen Concentration (ppm)
1	31.4 ± 2.7
2	20.4 ± 1.7
3	7.8 ± 0.7
4	3.3 ± 0.3

Table 3.4: Concentration of hydrogen measured in ReStoX gas phase on the first day.

In table 3.5 the results from the second measurements of ReStoX gas phase are compared to the expected values from the measurements of the individual bottles.

Impurity	Bottle Estimate (ppm)	ReStoX gas phase (ppm)
H ₂	0.06 - 0.10	0.50 ± 0.05
O ₂ + Ar	0.25 - 0.55	4.3 ± 0.4
N ₂	0.99 - 1.65	3.1 ± 0.4
Kr	0.003 - 0.025	0.050 ± 0.005
CH ₄	0.00 - 0.02	< 0.02
CO	0.00 - 0.21	< 0.2

Table 3.5: Comparison of estimate and ReStoX gas phase measurement.

The ReStoX gas phase impurities concentrations are consistently higher than the ones expected for the whole inventory. This result is expected, because the xenon boiling temperature is higher than the one of the other elements (see table A.1). While the xenon is liquid the other impurities are still gaseous. Looking at the boiling temperatures, one would expect all the impurities to be in the gaseous phase. However the impurities are partially dissolved in the liquid. The ratio between the concentration in the liquid and gaseous phase is called relative volatility and depends on the concentration of the components of the mixture, the temperature and other external factors such as the presence of a flow of gas or liquid. It is not possible to determine a priori the relative volatility coefficient for the mixture in ReStoX. For this reason, predicting the concentration of impurities in the liquid phase from the measurement of the gas phase is not possible.

This measurement is anyway an upper limit of the total concentration of impurities of the xenon inventory. The impurities are too high for normal operations of XENON1T but low enough to be purified via distillation.

3.5.2 Measurements of high air contamination

As already written in section 3.3, the xenon in the sample volume at the bottle rack is enough to repeat the measurement three times. Usually two measurements are performed to check the reproducibility. Only in rare cases when they are not consistent a third measurement is done. Inconsistent measurements of the same sample started to appear when bottles with a higher concentration of air were measured. There is no major difference in the setup or in the calibration chromatograms to indicate that the gas chromatograph causes this behaviour.

During the filling of xenon bottles ADDGXNH-1906661 and ADP65UF-859514, which contain a high amount of air, it was possible to take a xenon sample both at the beginning and when the bottle was emptied half way. The results of the four measurements are shown in figure 3.5 and summarised in table 3.6.

Meas nr (ppm)	1	2	3	4
H ₂	< 0.06	< 0.06	< 0.06	< 0.06
O ₂ + Ar	20.5 ± 0.7	15.0 ± 0.6	3.9 ± 0.2	2.9 ± 0.2
N ₂	62 ± 7	45 ± 5	12 ± 1	9 ± 1
Kr	/	/	0.04 ± 0.02	0.05 ± 0.02
CH ₄	/	/	< 0.03	< 0.03
CO	/	/	< 0.3	< 0.3

Table 3.6: Impurities concentration of different xenon measurements of bottles ADDGXNH-1906661 and ADP65UF-859514 at different times. It is impossible to measure the concentration of Kr, CH₄ and CO in the first two measurements due to the high nitrogen peak.

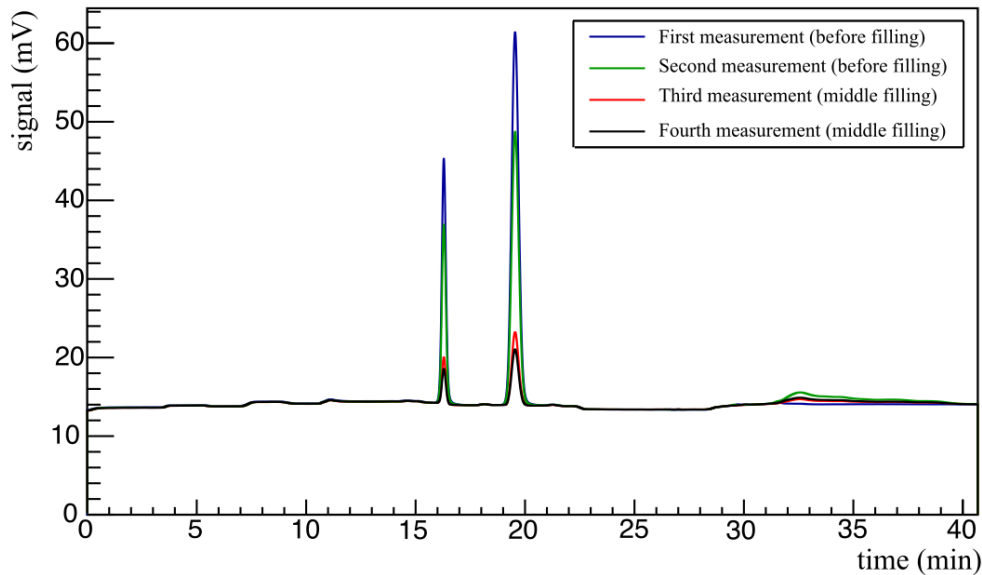


Figure 3.5: Chromatograms of different xenon measurements of the bottles ADDGXNH-1906661 and ADP65UF-859514 before and in the middle of the process of emptying. Blue and green measurements are measurements of the same sample of gas, taken before starting to fill the bottles. Red and black measurements are measurements of the same sample of gas, taken halfway during the filling of the bottles.

While the concentration of krypton, hydrogen, methane and carbon oxide are stable (or below sensitivity), oxygen, nitrogen and argon show a strong decreasing trend from measurement to measurement. One hypothesis for this behaviour is that the impurities in the bottles were not mixed from the start. The upper xenon, closer to the bottle valve, is more contaminated than the xenon in the center of the bottle. For this case, it is impossible to estimate the concentration by taking a sample only before emptying.

Furthermore, inconsistent measurements can be a result of inhomogeneous mixing of xenon samples from two bottles with different impurities concentrations. The sample first taken, which is closer to the valve of the xenon, might be more dirty. If the xenon flow in the bottle rack is mostly laminar, the dirty xenon is also the first to be measured, which can explain the trend seen from table 3.6.

3.6 Conclusion

In this chapter, a method to measure the contamination of krypton and electronegative impurities in the xenon prior to filling the xenon gas from the bottles into ReStoX has been shown. All the xenon bottles have been successfully measured and the validity of the provided certificates has been verified. As a consequence of those measurements, the bottles where a higher concentration of krypton were found have been distilled. The concentration of krypton in the xenon inventory is still higher of the one required to reach the background level specified for XENON1T. A long distillation run of the xenon inventory stored in ReStoX is scheduled before the start of the dark matter data taking.

A cumulative measurement of ReStoX gas phase has been done. The measured concentrations of the impurities are higher than the amount expected from averaging the measurements of the single bottles. The phenomenon is expected, but from this measurement it is not possible to find the concentration in the liquid phase. However, regarding the gas phase measurement as an upper limit for the whole xenon inventory, it was verified that it is possible to purify the xenon to reach the detector specifications.

During the campaign, some bottles showed inconsistent measurement of the same sample, especially when a high concentration of air was measured. One of the possible explanation is that the impurities in the xenon are not well mixed. Only bottles from the same company have been measured together, but it is possible that the impurity concentration in each bottle is different. If the impurities in two bottles are different the measurement only shows the sample taken closer to valve FV1218. This can lead to an underestimate of the impurities of the bottle that is farther from the xenon sample volume and an overestimate of the impurities in the bottle that sits the closest. The time scale of the sample taking procedure is minutes (never exceeding 15 minutes), while the time scale expected from gas mixing in a laminar regime is longer. The second half of this work focuses on studying the time scale of gas diffusion and establish if it is a possible cause for inconsistent measurements.

Chapter 4

Gas mixing measurements

After the inconsistent measurements from chapter 3, a dedicated study has been done on gas diffusion. The goal of this chapter is to characterize the time scale of gas mixing and find the best speed-up mean. The study is performed on a one dimensional system. A gas with impurities is injected on one side of the system, and the evolution of the concentration of the impurities is measured at the other side where there is pure gas at the beginning. Two tests with two different bulk gas have been done. The first preliminary test has been performed with argon and a mixture of argon and methane. Then a final test with xenon and a gas mixture containing xenon, methane, oxygen and krypton has been carried out.

By measuring the evolution of the concentration of the impurity gases, it is possible to determine the time scale of mixing. The expectation is to see the impurities' signal increase until it reaches a saturation level when the two gases are completely mixed. It is possible to calculate the time needed for mixing and to compare it after performing different operations.

In this chapter, first a preliminary theoretical overview is given. Then the experimental setup and the analysis method are introduced. Finally the results of the argon test are described, and followed by results obtained with xenon.

4.1 Theoretical background

The diffusion of a gas is caused by a difference in temperature, pressure and, in case it is a gas mixture, concentration of the components [48]. For a binary gas mixture, the time evolution of the concentration of one of the components is given by the differential equation

$$\frac{\partial C}{\partial t} = D^C \cdot \nabla^2 C + D^T \cdot \nabla^2 T + D^p \cdot \nabla^2 p \quad (4.1)$$

where C is the concentration of the observed element, T is the temperature, p is the pressure ∇ is the Laplace operator and D^C , D^T and D^p are the diffusion coefficients for concentration, temperature and pressure respectively. For our measurements at the bottle rack we can assume that the temperature and the pressure are constant. Therefore there is no diffusion due to the pressure and temperature gradient, and the only term left in equation 4.1 is

$$\frac{\partial C}{\partial t} = D \cdot \nabla^2 C \quad (4.2)$$

with $D^C \equiv D$. This equations is known as the second law of Fick [49]. In the case of the diffusion inside a pipe, we can approximate the 3 dimensional problem to a 1 dimensional one. We can drop the ∇ operator and use the second partial derivative with respect to one spatial dimension.

$$\frac{\partial C(x, t)}{\partial t} = D \cdot \frac{\partial^2 C(x, t)}{\partial x^2} \quad (4.3)$$

Equation 4.3 is the heat equation. The initial conditions needed to solve equation 4.3 are discussed later.

A crucial part of the calculation is the determination of the diffusion coefficient D . For an ideal gas, the diffusion coefficient of a binary system can be calculated with the formula [50]

$$D_{AB} = \frac{13}{16} \frac{(4\pi k T M_{AB}^{-1})^{1/2}}{n \pi \sigma_{AB}^2 \Omega_D} f_D \quad (4.4)$$

where $M_A, M_B =$ masses of the two components (in amu)

$$M_{AB}^{-1} = (1/M_A + 1/M_B)^{-1}$$

$n =$ Number density of molecules in the mixture

$k =$ Boltzmann constant

$T =$ Temperature (in K)

$\Omega_D =$ Collision integral for diffusion (dimensionless, model dependant)

$\sigma =$ Characteristic length of the intermolecular force law (model dependant)

$f_D =$ Correction factor when $M_A \ll M_B$, and A is present at trace amount

$f_D \simeq 1.1$ [50] when one element is much heavier than the other and the light element is present only at trace amount. This are in principle the conditions we have: a heavy element (xenon) and impurities present at trace amount. $\sigma_{AB} = \frac{\sigma_A + \sigma_B}{2}$, where σ_A is the diameter of the sphere containing the molecule.

Using $f_D = 1.1$ and the law of ideal gas to express n as a function of the pressure, equation 4.4 becomes

$$D_{AB} = \frac{0.002926 T^{3/2}}{p M_{AB}^{1/2} \sigma_{AB}^2 \Omega_D} \quad (4.5)$$

To calculate the collision integral and the characteristic length, the Lennard-Jones potential model is employed. This model describes the viscosity of a gas with intermolecular forces. The values of σ and ϵ are determined experimentally from the viscosity of pure gases. Their value for the gases used in this work are listed in appendix A.1. Ω_D is a function of $T^* = kT/\epsilon_{AB}$, where $\epsilon_{AB} = (\epsilon_A\epsilon_B)^{1/2}$, and its equation has been empirically found to be

$$\Omega_D = \frac{A}{(T^*)^B} + \frac{C}{\exp(DT^*)} + \frac{E}{\exp(FT^*)} + \frac{G}{\exp(HT^*)} \quad (4.6)$$

with $A = 1.06036$, $B = 0.15610$, $C = 0.19300$, $D = 0.47635$, $E = 1.03587$, $F = 1.52996$, $G = 1.76474$ and $H = 3.89411$ [50]. Table 4.1 lists the diffusion coefficients calculated for the gas mixtures used in this work.

Element A	Element B	D_{AB} (cm ² /s)
Ar	CH ₄	0.2314
Xe	He	0.2391
	CH ₄	0.1093
	O ₂	0.0936
	Kr	0.0810

Table 4.1: Diffusion coefficients of the gas mixtures used.

There are two more assumptions made. First, the formula is valid for a binary system, while in our setup we have xenon as main gas and many other elements present at trace amount. Since the concentrations of the elements are very low it is assumed that each of the component of the mixture behaves like it interacts only with xenon. The second assumption is that the mixture is an ideal gas. This is not true for the bottle rack setup, since the critical point of xenon is at room temperature and the pressure of xenon in one bottle is around 60 bars.

Even without solving the equation, from the values of the diffusion coefficient it is possible to have an idea how different elements diffuse with respect to each other. In particular, from equation 4.5 $D \propto M^{-1/2}$, so the bigger the elements, the slower the diffusion. Since xenon is the heaviest of the considered elements, it is also the slowest to diffuse, while lighter elements such as argon or helium are much faster.

To solve equation 4.3 one initial condition and two boundary conditions are needed. As initial condition, we chose a sigmoid function with equation

$$S(x; s, l) = \frac{1}{1 + \exp(s \cdot (x - l/2))} \quad (4.7)$$

where s is the smearing parameter of the curve and l is the length of the pipe of the one dimensional system we are considering. In our setup we have half of the pipe filled with pure gas and the other side filled with a mixture of gas and impurities, so the sigmoid function is a good approximation. The system is insulated (there is no exchange of gas outside of the pipe), so the boundary conditions are

$$\left. \frac{\partial C}{\partial x} \right|_{x=0} = 0; \quad \left. \frac{\partial C}{\partial x} \right|_{x=l} = 0 \quad (4.8)$$

It is possible to solve equation 4.3 by the technique of separation of variables [51]. Writing $C(x, t) = X(x)T(t)$, equation 4.3 becomes

$$\frac{1}{DT} \frac{dT}{dt} = \frac{1}{X} \frac{d^2 X}{dx^2} = -\frac{1}{a^2} \quad (4.9)$$

where a is a constant. The solutions for the separated functions are

$$\begin{aligned} T(t) &= A \exp(-Dt/a^2) \\ X(x) &= B \cos(x/a) + C \sin(x/a) \end{aligned}$$

where A , B and C are constant. Combining them together gives the general solution for $C(x, t)$

$$C(x, t) = e^{-Dt/a^2} \left[E \cos\left(\frac{x}{a}\right) + F \sin\left(\frac{x}{a}\right) \right] \quad (4.10)$$

Using the boundary conditions (4.8), it is found that $E = 0$ and $a = l/n\pi, n \in \mathbb{N}$. Considering also the initial condition, equation 4.10 becomes

$$C(x, t) = \frac{c_0}{2} + \sum_{n=1}^{\infty} c_n \cos\left(\frac{n\pi x}{l}\right) e^{-Dt(m\pi/l)^2} \quad (4.11)$$

with

$$c_m = \frac{2}{l} \int_0^l \cos\left(\frac{m\pi x}{l}\right) S(x; l, s) dx \quad (4.12)$$

There is no explicit analytic form for equation 4.11. However, it was tested that it is possible to truncate the infinite series with a small error.

4.2 Experimental setup

Figure 4.1 shows the scheme of the experimental setup. The goal is to reproduce a smaller scale and simplified version of the bottle rack. Instead of four bottles,

two bottles are connected at the ends of a pipe, which is called here the mixing volume. In order to regulate the amount of gas inserted into the mixing volume, two small pipette volumes are used.

At the right of the mixing volume there is a pressure sensor. The total amount of gas inserted in the system is such that the total pressure is less than 3 bars, much less compared to the bottle rack. There is in addition a temperature sensor placed on the outside of the mixing volume, not represented in figure 4.1. In order to measure the gas composition, a Quadrupole Mass Spectrometer (Pfeiffer Vacuum M 200, QMS in the following) has been used. For a detailed description of the mass spectrometer, see appendix B.

The QMS is a low pressure spectrometer. It is connected to a vacuum chamber. The chamber has a vacuum gauge and a variable leak valve (Agilent Technologies) to regulate the input sample (figure 4.2 shows the inner setup). At the bottom of the vacuum chamber there is a turbo molecular pump (Agilent Technologies).

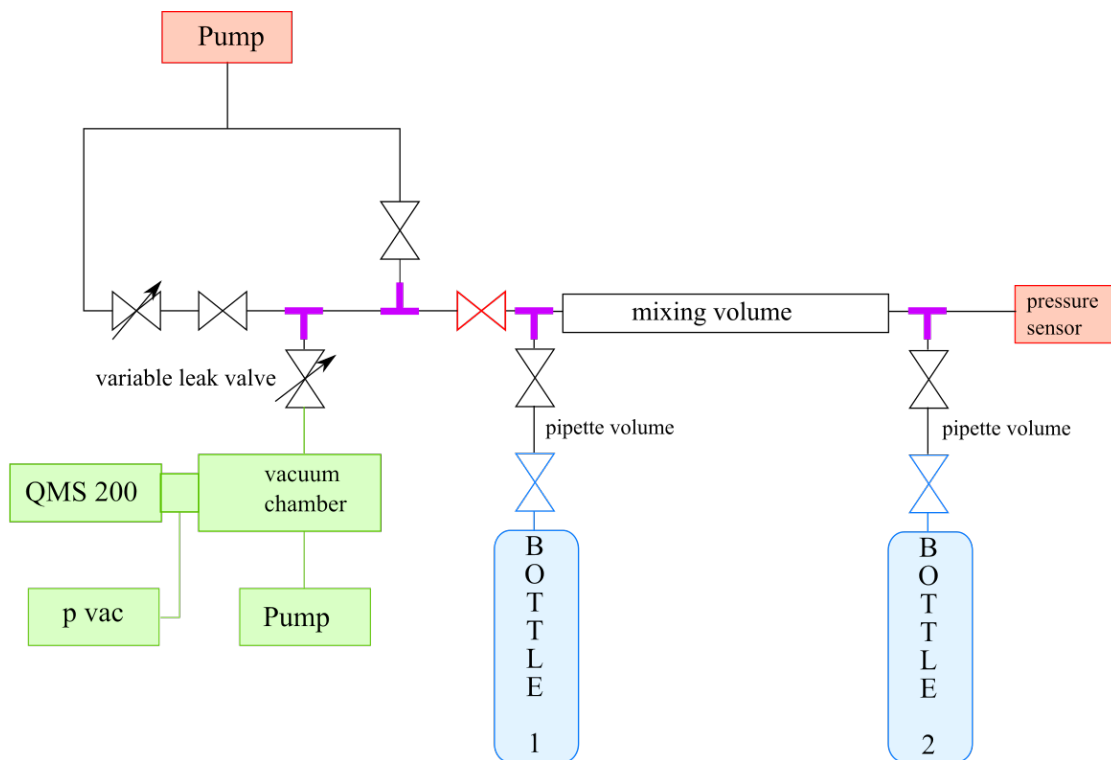


Figure 4.1: Scheme for gas mixing measurements. The mixing volume is a stainless steel pipe 50 cm long and with an internal diameter of 11 mm, the same inner diameter as a 1/2 inch VCR connection. The red valve was added at a later time. Highlighted in purple are the T-connectors.

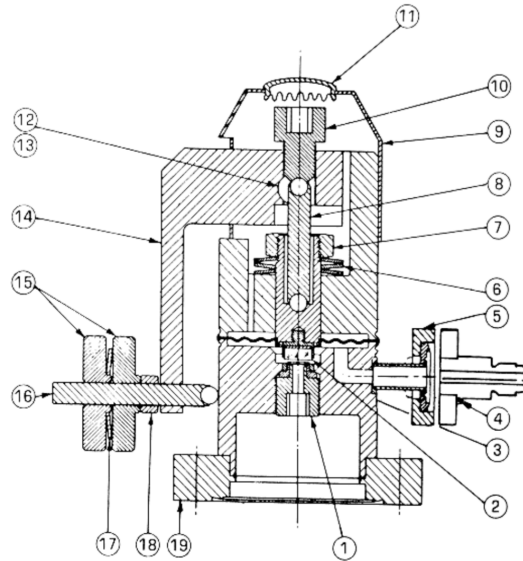


Figure 4.2: Details of the inner setup of the variable leak valve model 951-5106 from Agilent Technologies. Figure taken from ref [52].

Two series of gas mixing tests have been performed. First a series of tests with argon 5.0 and a mixture of 90% argon and 10% methane (with both the bottles at 12 bars at the start of the experiment). The second series was performed with gettered xenon and a custom mixture of xenon, 3% oxygen, 3% methane and 3% krypton. Bottle 1 from figure 4.1 contains the pure element, while bottle 2 contains the mixture.

4.3 Procedure

The mixing procedure is the same for both tests. Before the beginning of each test, the system was baked and pumped until $p_{vac} = 2.7 \times 10^{-8}$ mbar and $p = -1$ bar (underflow). At the beginning of the test, the sample from the pure gas bottle is expanded in the mixing volume, so that the pressure is $p \simeq 0.4$ bar (relative), which is 1.3 bar absolute. Then the sample from the mixture bottle is added, for a total $p \simeq 1.7$ bar (relative) or 2.6 bar absolute. To control the amount of gas put inside the mixing volume, the pipettes volumes are used. Between 3 and 4 pipettes were taken from each bottle for each measurement. Since the pressure inside the bottles and the pipettes volume are similar, this procedure should lead to the same amount of the two gases in the mixing volume. The initial situation should be that the right half of the mixing volume is filled with pure gas, and the left half is filled with gas mixed with the impurities. The impurities density

is close to the sigmoid function, used as initial condition to solve the differential equation in section 4.1. This is a “worst case” scenario compared to the bottle rack operations: in the bottle rack the pipettes volumes are opened in small steps and it is expected that the two gases are partially mixed at the beginning.

Once the gas mixture is set in the mixing volume, the data acquisition starts. The data acquisition procedure is different in the two tests. In the argon-methane measurements, the variable leak valve is open to the target pressure $p_{vac} \simeq 1 \times 10^{-6}$ mbar and the data acquisition is started. After the end of the measurement, the leak valve is closed in order not to lose gas. A measurement is taken every 20 to 40 minutes.

In the xenon tests, the leak valve has been opened until $p_{vac} \simeq 1 \times 10^{-6}$ mbar and then left open. The data acquisition method was updated so that the software takes a scan of the masses between 0 and 90 amu every 30 minutes. Since the valve is open, a small amount of gas is lost over time. However, the loss is very small and negligible in a 2 day interval, a typical running time of a test. The advantage of this method is that there are no more data taking interruption in a 48 hours interval.

4.4 Analysis

The first step is to identify and quantify the peaks in the mass spectrums. The peaks of interest are at different masses, depending on the test. After identifying the peaks, a graph of the relative concentration vs time is calculated. The expectation is to have the impurities signal to increase and the pure gas signal to decrease over time. The signal of the bulk gas has not been analyzed: the error of the signal is proportional to the height of the peak, and the bulk gas, since it is the main component of the mixture, has the highest peaks.

Figure 4.3 shows a spectrum for a typical background measurement. The peaks at position 0 and 2 amu are noise peaks and change shape from measurement to measurement. Since hydrogen falls in this region, it is not possible to quantify it. The cluster of peaks between masses 15 and 20 is due to water and its fragments, OH^- and O. The other notable peaks are nitrogen and carbon monoxide (mass = 28 amu), oxygen (mass = 32 amu) and argon (mass = 44 amu). The background peaks are around 2 orders of magnitude less than the signal peaks.

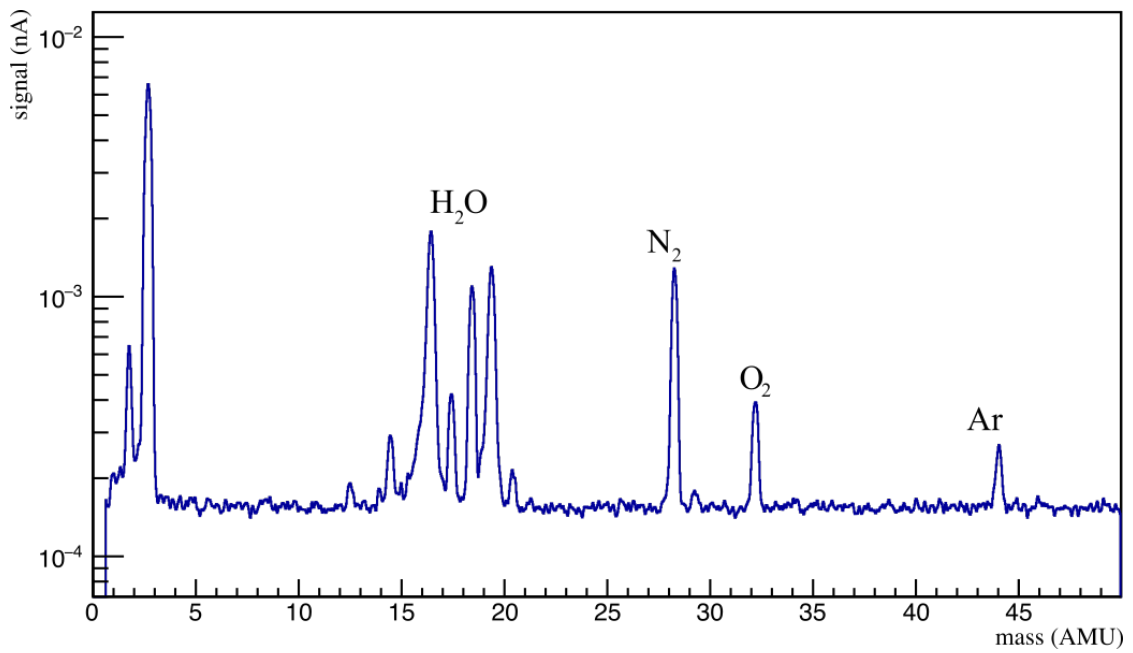


Figure 4.3: Background spectrum.

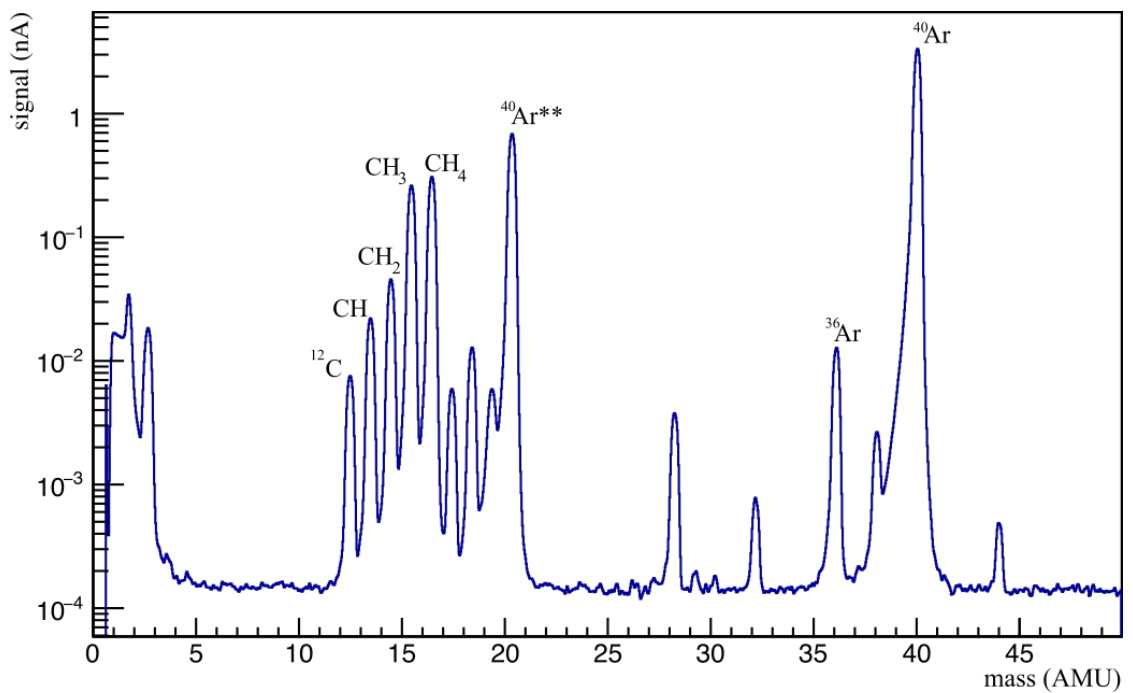


Figure 4.4: A mass spectrum for the argon-methane mixing test.

Figure 4.4 shows a spectrum for an argon-methane measurement. Methane is broken in hydrocarbon fragments and has 5 peaks: CH_4 (mass = 16 amu) and the fragments CH_3 (mass = 15 amu), CH_2 (mass = 14 amu), CH (mass = 13 amu) and ^{12}C . The background peaks are 3 order of magnitude smaller than the signal peaks, so no influence of the background on the data is expected. The argon peaks are ^{40}Ar , ^{38}Ar , ^{36}Ar and double ionized ^{40}Ar (at 20 amu). ^{40}Ar , the most abundant isotope, is the highest signal.

The interesting peaks for the xenon tests are labelled in figure 4.5. In addition to the peaks of methane discussed above, also the O_2 peak and the ^{84}Kr , the most abundant isotope of krypton, are monitored. Single ionized xenon is not visible on this spectrum, since it has a mass outside the range of the measurement. However, xenon can be detected if its amount is high enough to trigger double or triple ionization phenomena (see appendix B).

To quantify the signal, the area of the peaks is used. A gaussian fit function has been employed to determine the signal region. The area is integrated over a 3σ interval, which includes 95% of the peak. The peak tails, which are not gaussian, are negligible. The width of the gaussian is fixed and constant for every peak. The mean of the peaks, corresponding to the mass of the gas, is constant and stable in

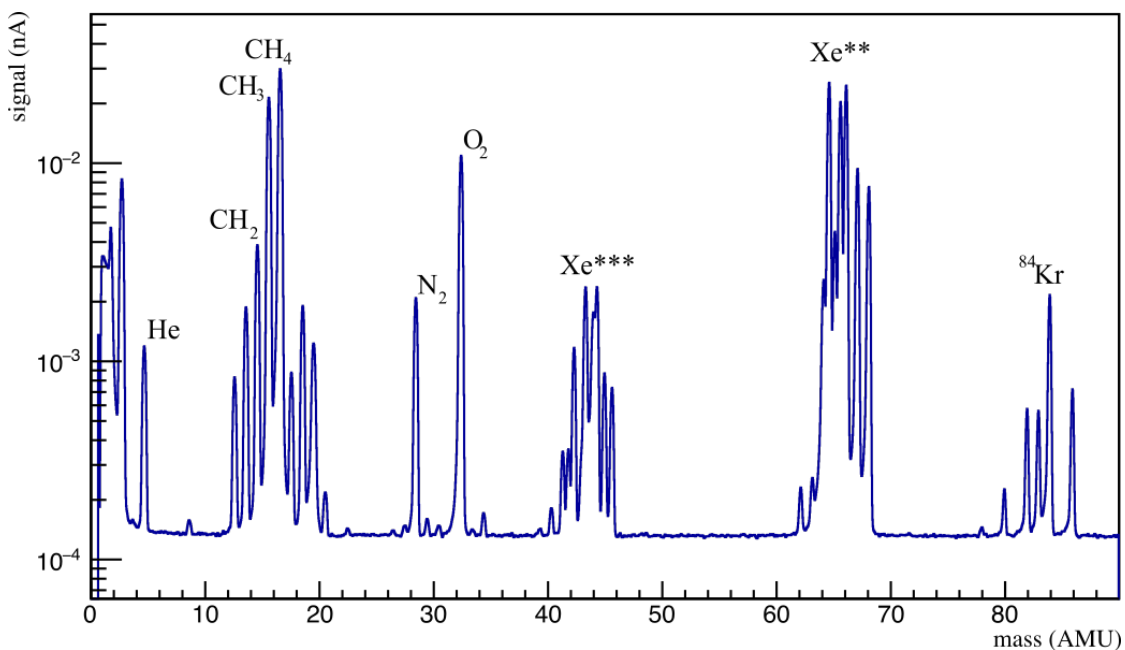


Figure 4.5: A mass spectrum for the xenon mixing test. Since the xenon isotopes have a mass between 124 and 136 amu, the single ionized signal is not in the spectrum. However, it is still possible to detect double and triple ionized xenon in the measured range.

all the measurements, with 0.5 offset between 4 amu (He) and 136 amu (Xe).

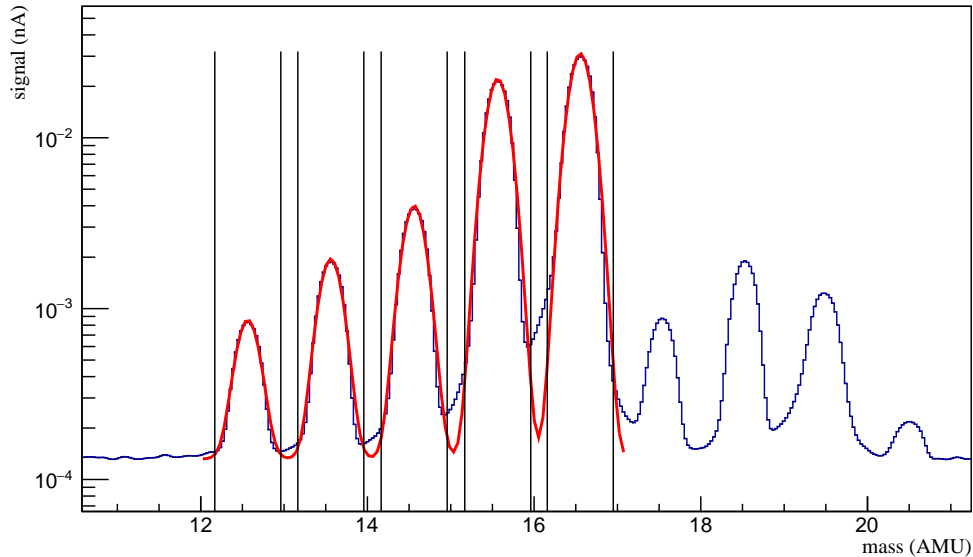


Figure 4.6: Fit (red) and integration intervals (black) for a xenon spectrum of the methane region. The integration intervals don't overlap with each other and the influence of the peaks on the adjacent ones is negligible.

To evaluate the baseline, a linear fit on a peak free region is performed. The area of the peak is computed by subtracting the area of the fitted baseline from the area of the peak region in the 3σ interval. The integration interval is small enough that the contamination of neighbour peaks is less than 1% if the two peaks have comparable areas. This has been estimated for this analysis.

The signal is plotted then over time. The maximum height of the signal is reached at equilibrium and it is used for normalization.

The dominant error is the systematic concentration variation from test to test due to the different amount of gas introduced into the system. Since the valves are hand operated, the pressure is not always perfectly constant. Consequently, the two fraction of gas are not always equal and the plateau height changes from measurement to measurement. For each series of test, the error is calculated from the distribution of the final plateau heights.

To compare the different data sets, the time when 80% or more of gas is mixed (t_{80}) is calculated. The error on the time is given by the difference of the first and the last point that cross the 80% line plus additional 15 minutes since the data are taken every 30 minutes. The fit function 4.11 only works for simple models,

and can't be used for modelling data when a speed up operation performed. The fit has been done only the data of the xenon tests with no mixing operation.

4.5 Results

4.5.1 Argon test

Figure 4.7 shows the data of the first argon tests for the CH peak at mass 13 amu. The main problem with the data acquisition procedure is that there are big holes in the graph due to the absence of data taking during night. To check for reproducibility and fill the data holes, the test has been repeated three times. The only data set that fully covers the 0.8 concentration region is the black one. This measurement is used as control data to compare the mixing operations performed afterwards. The t_{80} for the methane fragments of the control measurement are listed in table 4.2. This long mixing time confirms the hypothesis that the measurements of the xenon samples from the four bottles in the bottle rack are not well mixed. As seen from the diffusion coefficients (see table 4.1), we can expect that, when one of the gas is xenon, the equilibrium is reached even slower.

Gas	Atomic mass	t_{80} (hours)
^{12}C	12	5.9 ± 0.6
CH	13	6.5 ± 0.6
CH ₂	14	5.9 ± 0.9
CH ₃	15	6.5 ± 0.9
CH ₄	16	5.9 ± 0.9

Table 4.2: Results of t_{80} for the monitored peaks in the control measurement for the argon test.

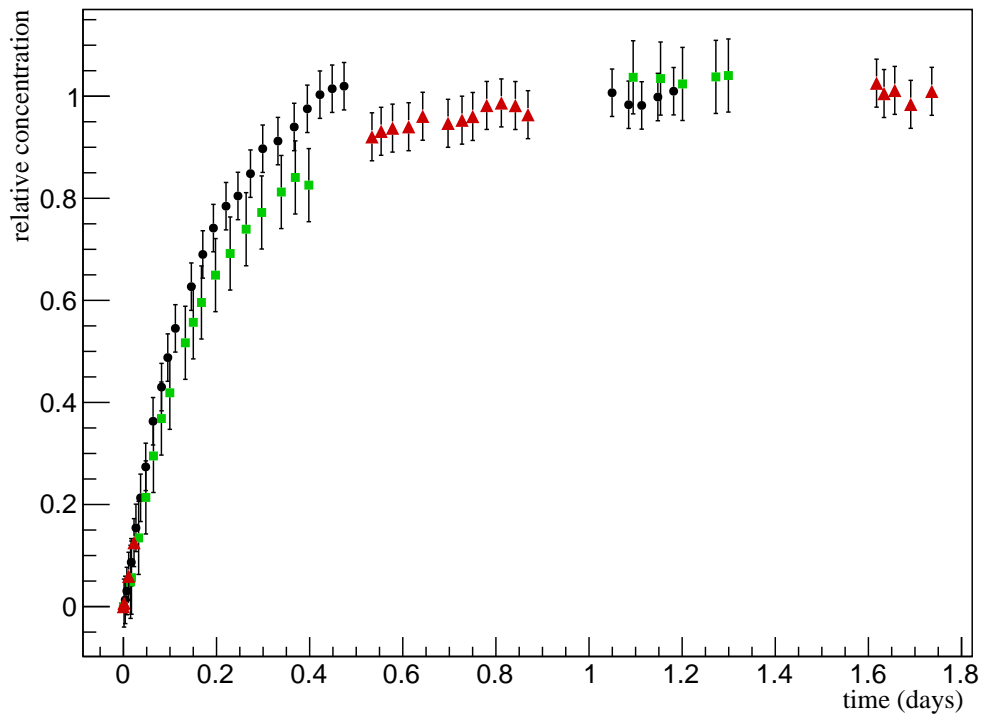


Figure 4.7: Three argon methane mixing measurements, performed on different days. Data for CH peak (mass = 13 amu).

Since waiting several hours for the xenon to be mixed is not possible for the timetable of XENON1T, several mixing options have been tested. The first one is increasing the temperature: since the diffusion coefficient is related to the temperature $D \propto T^{3/2}$, increasing the temperature is supposed to accelerate the process. The test was repeated with baking the pipe at 85°C . The data is shown in figure 4.8 (in red), compared to the control measurement (black). The data does not cover the 0.8 line but it looks similar to the control data set, where no baking was applied. Baking didn't help improve the mixing time since the dependence of the diffusion coefficient is not big enough.

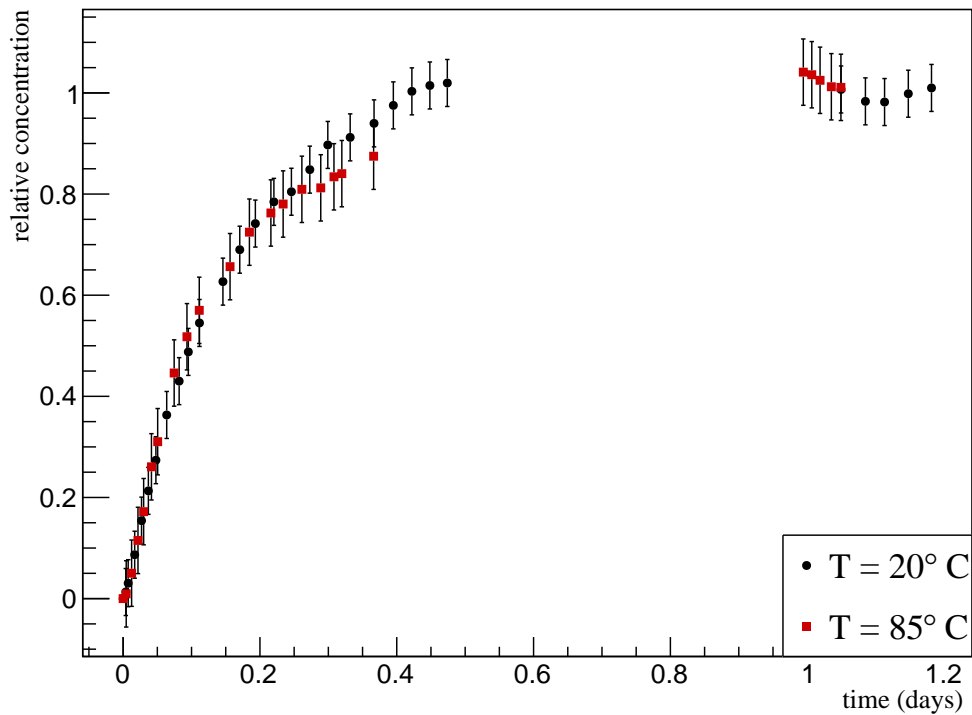


Figure 4.8: Black: control data set with no speeding operation performed. Red: mixing with increasing the temperature up to 85°C. Data for CH peak (mass = 13 amu).

In a second test, a steel ball of 8.5 mm diameter has been inserted inside the pipe. Two magnets are used to move it along the pipe and in the T-connectors (see figure 4.1). The procedure was mixing for 5 minutes, open the leak valve to measure the sample, then close it and mix for another 5 minutes. This procedure has been performed 5 times, for a total mixing time of 25 minutes, then the mixing was stopped and the sample was measured as in the previous cases. Figure 4.9 compares the result of this procedure to the no action one. Also in this case it is not possible to estimate t_{80} . However, the mixing appears even slower compared to the control data set.

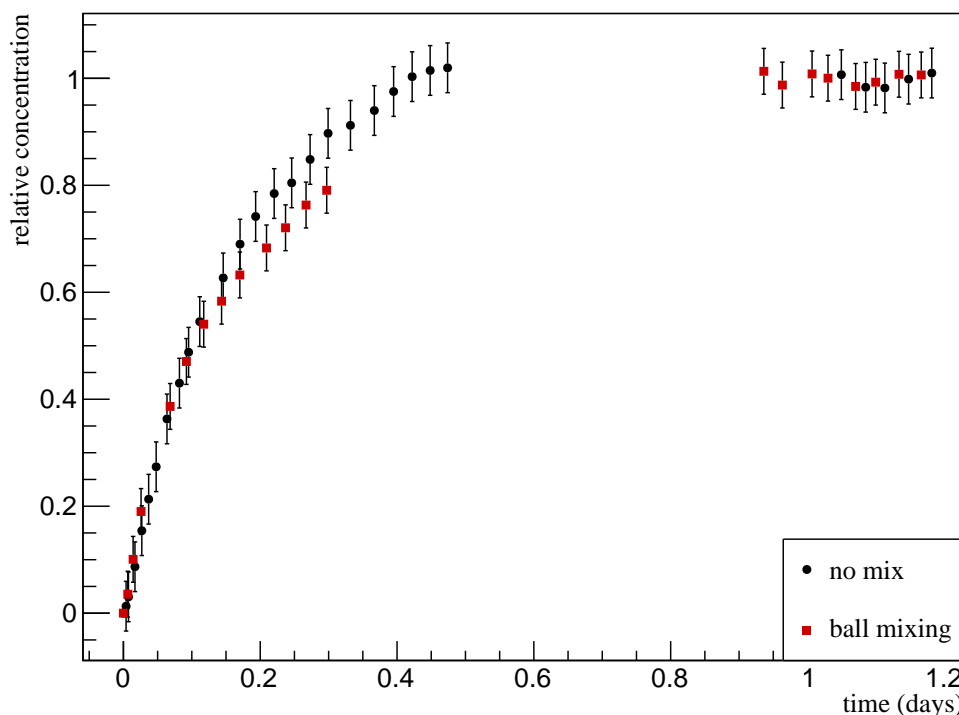


Figure 4.9: Black: control data set with no speeding operation performed. Red: mixing with the steel ball. Data for CH peak (mass = 13 amu).

One possible explanation of this unexpected result is the internal structure of the leak valve (see figure 4.2). The valve has many capillaries with small section: the steel ball is too big to go inside and the small section slows down the gas diffusion inside. To check this hypothesis, an additional valve before the leak valve has been added to the setup (the valve drawn in red in figure 4.1). Since the steel ball is too big to go through a valve, it is not possible to take data during the mixing, since the gas in the volume on the left side of the red valve can not be mixed once the red valve is open. Instead of many small steps, the steel ball mixing has been done in one time for 25 minutes. Figure 4.10 shows the graph of this last test compared to the previous one. It shows that the gas is already above the 0.8 line when the first data point is taken. 25 minutes of mixing with a steel ball almost completely mix the two gases.

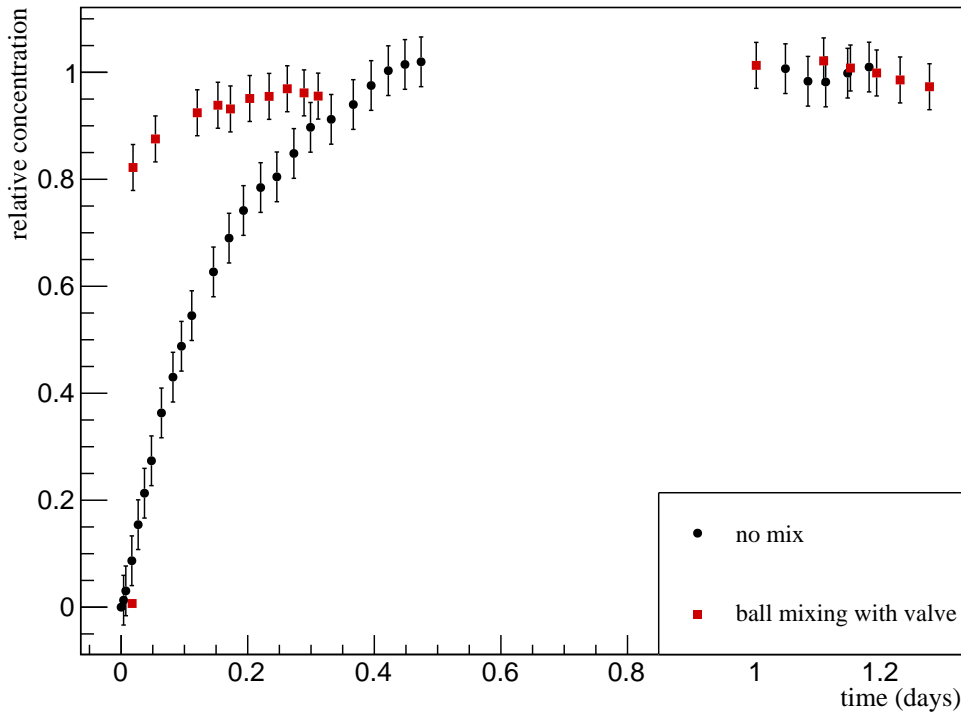


Figure 4.10: Black: control data set with no speeding operation performed. Red: mixing with the steel ball and the extra valve added. Data for CH peak (mass = 13 amu).

4.5.2 Xenon test

Since the last steel ball mixing test with argon was successful, in the xenon series only this method was employed. Four tests have been performed with xenon. First a control test with no mixing operations, where the red valve in figure 4.1 is open from the beginning. Second a test with the red valve initially closed and no mixing with the steel ball. The red valve is open after expanding the gas in the pipe. Third, a test starting with the red valve closed, mixing with the steel ball for 5 minutes and then opening the red valve, and last one mixing for 20 minutes before opening the valve. Each measurement has been repeated twice.

In the first tests with no mixing operations performed, it was possible to fit the data using function 4.11. The fit was performed fixing the length of the pipe at 80 cm (as measured from the experimental setup) and the c_0 parameter at 1, as expected from the equilibrium conditions. Figure 4.11 shows the fit for one mass and the results of the diffusion coefficient and the smearing parameter are listed

in table 4.3.

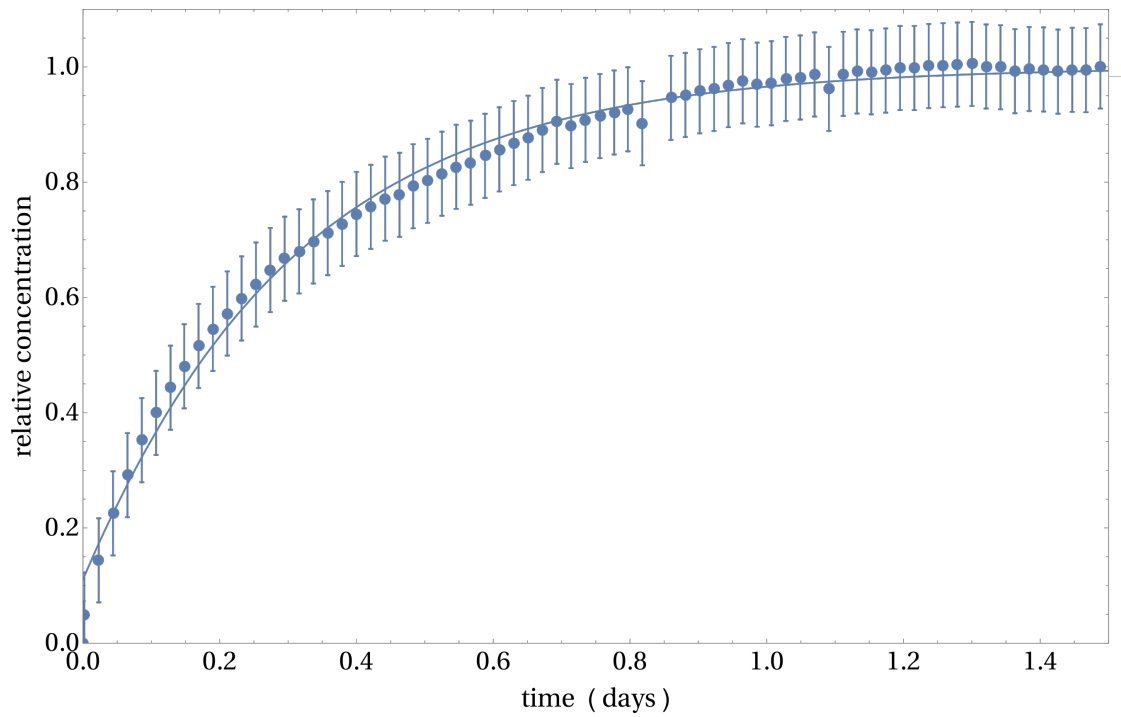


Figure 4.11: Fit with function 4.11 for a no mixing xenon data set with mass = 32 amu (O_2).

For the other tests, it was not possible to employ the fit, since no model has been found to account for active mixing. To compare the timescale for the different mixing scenarios, the time when the impurities signal exceeds 80% of the total of its equilibrium concentration is employed (t_{80}), as used with the argon tests. Table 4.4 lists the t_{80} obtained in the different mixing tests. Figures 4.12, 4.13a and 4.13b show 3 of the data sets for each operation.

Data set	Gas	Mass (amu)	Diffusion coefficient (cm ² /s)	Curve smearing (1/cm)
1	¹² C	12	0.0267 ± 0.0007	0.066 ± 0.002
	CH	13	0.0285 ± 0.0006	0.076 ± 0.002
	CH ₂	14	0.0284 ± 0.0006	0.071 ± 0.002
	CH ₃	15	0.0288 ± 0.0006	0.078 ± 0.002
	CH ₄ /O ₂	16	0.0283 ± 0.0006	0.073 ± 0.002
	O ₂	32	0.0245 ± 0.0004	0.076 ± 0.002
	⁸⁴ Kr	84	0.0210 ± 0.0005	0.061 ± 0.002
2	¹² C	12	0.0284 ± 0.0007	0.063 ± 0.002
	CH	13	0.0293 ± 0.0005	0.077 ± 0.002
	CH ₂	14	0.0292 ± 0.0005	0.072 ± 0.002
	CH ₃	15	0.0292 ± 0.0005	0.078 ± 0.002
	CH ₄ /O ₂	16	0.0285 ± 0.0005	0.070 ± 0.002
	O ₂	32	0.0243 ± 0.0004	0.074 ± 0.002
	⁸⁴ Kr	84	0.0169 ± 0.0003	0.059 ± 0.001

Table 4.3: Fitted values of the diffusion coefficient (D) and the initial condition curve smearing from the fit.

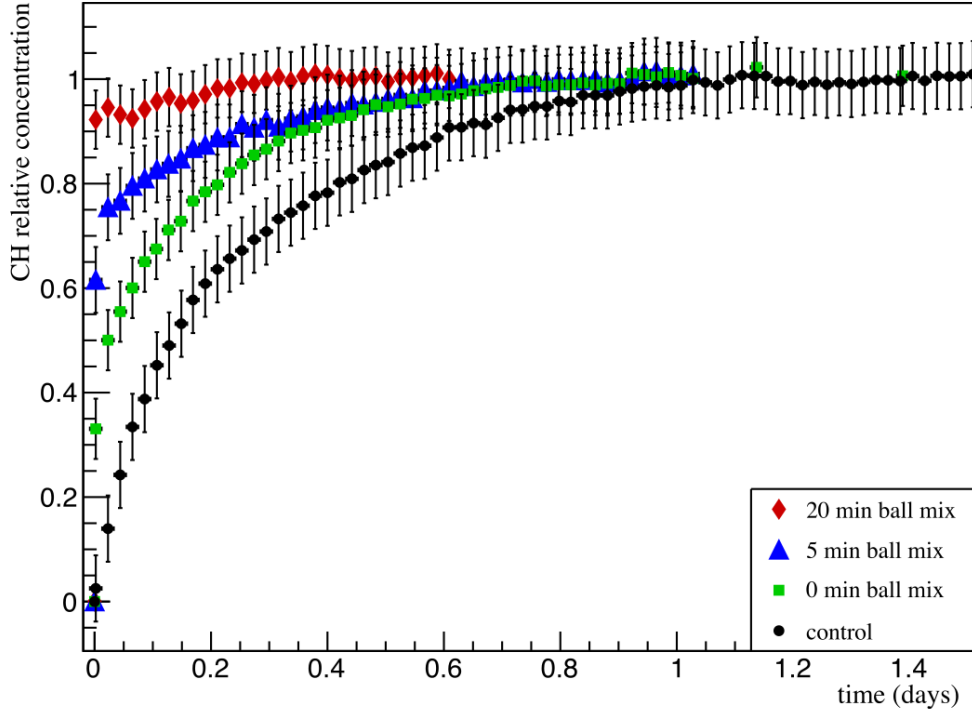


Figure 4.12: Black: control data set with no speeding operation performed. Green: 0 minutes mixing then opening valve V5. Blue: 5 minutes mixing then opening the valve. Red: 20 minutes mixing then opening the valve. Data for CH peak (mass = 13 amu).

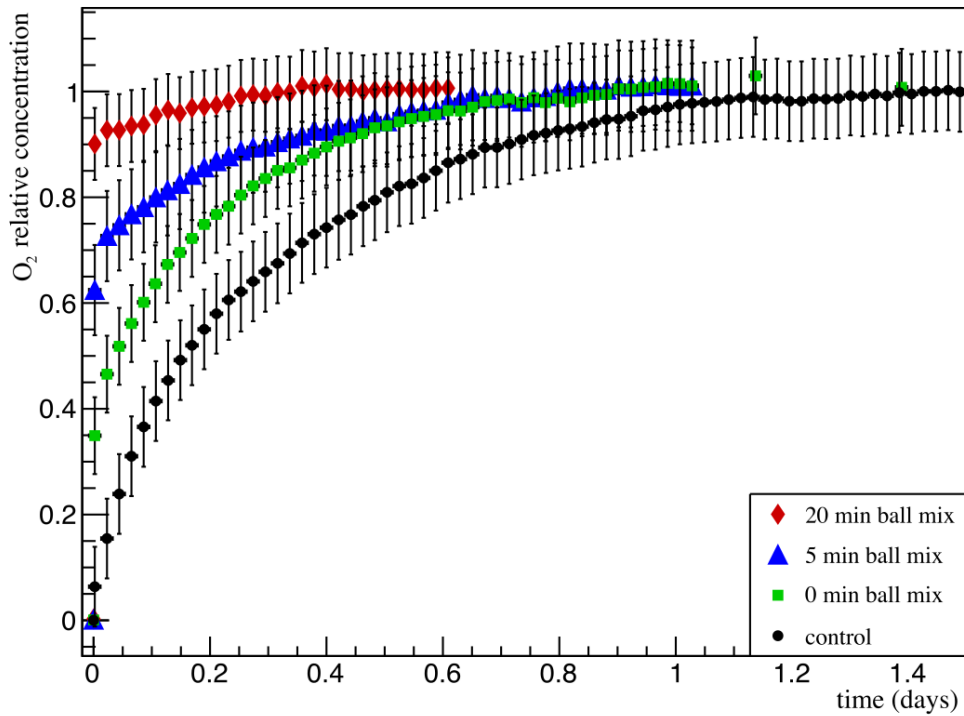
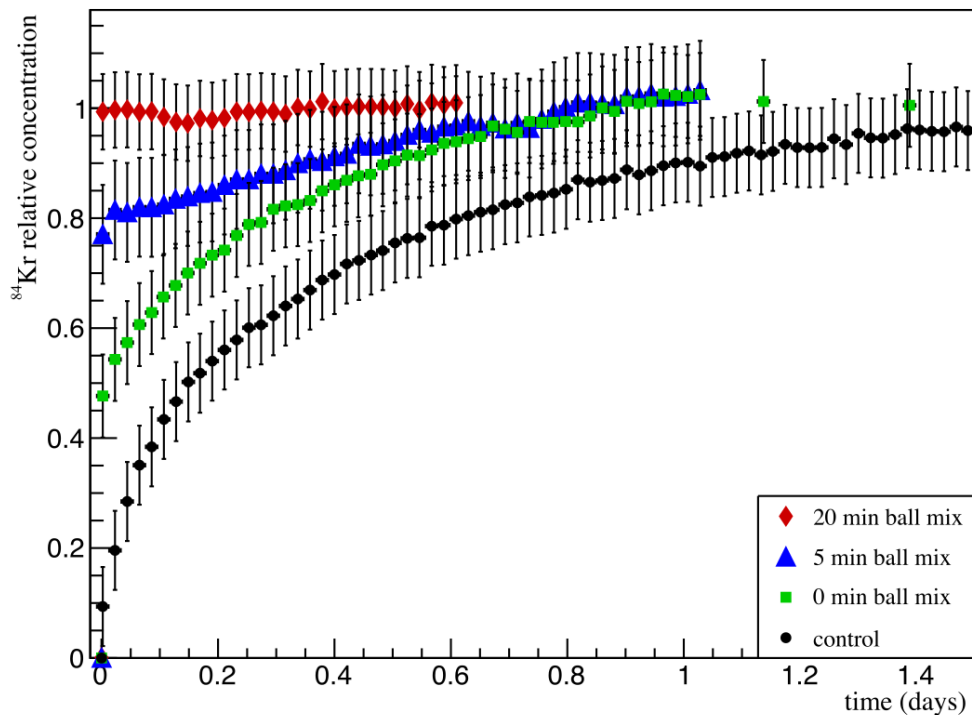
(a) Data for O_2 peak (mass = 32 amu).(b) Data for ^{84}Kr peak (mass = 84 amu).

Figure 4.13: Black: control data set with no speeding operation performed. Green: 0 minutes mixing then opening valve V5. Blue: 5 minutes mixing then opening the valve. Red: 20 minutes mixing then opening the valve.

The valve opening test has been done to test the effect of opening one valve on the mixing. This effect is still present in the bottle rack. The valve opening accelerates the process, but the ball mixing contributes the most.

4.6 Conclusion

The tests performed in this chapter show that slow gas mixing may cause incorrect and inconsistent measurements. The argon tests give a strong indication that mixing with a steel ball can decrease the mixing time down to 20 minutes. The tests have been repeated with xenon, and they confirm the result. A steel ball has been introduced in the bottle rack in the volume between valves FV1216 and FV1218 of figure 2.8c and used for the last xenon bottles measurements.

The big unavoidable systematic error due to the different amount of gas poured in the mixing volume causes the setup to not be sensitive enough to distinguish the different t_{80} for the elements in the xenon mixture. However, it is possible to compare t_{80} of the methane in argon and xenon tests. For the argon-xenon test the average $t_{80} = (10.5 \pm 0.2)$ hours, while for the argon-methane tests the average $t_{80} = (6.2 \pm 0.3)$ hours. This is in agreement with the prediction from theory, which states that diffusion is faster if the radius of the molecules is smaller.

An explicit fit function has been found for a simple one dimensional problem. The results for the diffusion coefficient found by the fit in the xenon measurements (table 4.3) are roughly twice the values calculated from the theory (table 4.1). The possible explanation for this discrepancy is that the model we use describes partially the gas system. The main differences are that the model has just one dimension and doesn't account for the inner configurations of the valves and the presence of the T-connectors. In addition, it is impossible to determine precisely the starting conditions of the system. The fact that the diffusion coefficients from the fits are bigger than the one expected from theory is an indication that the gas at the beginning is more mixed than the initial function takes into account.

Gas	Mass (amu)	Control 1 t_{80} (h)	Control 2 t_{80} (h)	0 min mixing 1 t_{80} (h)	0 min mixing 2 t_{80} (h)
^{12}C	12	11.0 ± 1.0	9.6 ± 0.7	5.0 ± 0.5	5.0 ± 0.5
CH	13	11.5 ± 0.7	10.1 ± 0.7	5.5 ± 0.5	5.5 ± 0.5
CH_2	14	10.6 ± 0.7	10.6 ± 0.5	5.5 ± 0.5	5.5 ± 0.5
CH_3	15	11.0 ± 0.5	10.1 ± 0.5	5.0 ± 0.5	5.0 ± 0.5
CH_4/O	16	10.1 ± 0.5	10.6 ± 0.7	5.5 ± 0.5	5.5 ± 0.5
O_2	32	10.6 ± 0.7	11.0 ± 0.7	5.0 ± 0.5	5.0 ± 0.5
^{84}Kr	84	10.6 ± 0.5	10.1 ± 0.7	5.5 ± 0.5	5.5 ± 0.5
Gas	Mass (amu)	5 min ball mixing 1 t_{80} (h)	5 min ball mixing 2 t_{80} (h)	20 min ball mixing 1 t_{80} (h)	20 min ball mixing 2 t_{80} (h)
^{12}C	12	2.6 ± 1.0	1.7 ± 0.7	< 0.2	< 0.2
CH	13	3.1 ± 0.5	2.2 ± 0.7	< 0.2	< 0.2
CH_2	14	2.6 ± 0.5	2.6 ± 0.2	< 0.2	< 0.2
CH_3	15	2.6 ± 0.5	2.2 ± 0.5	< 0.2	< 0.2
CH_4/O	16	2.6 ± 0.5	2.6 ± 0.2	< 0.2	< 0.2
O_2	32	2.6 ± 0.5	2.2 ± 0.7	< 0.2	< 0.2
^{84}Kr	84	4.1 ± 1.0	2.2 ± 0.2	< 0.2	< 0.2

Table 4.4: Results of t_{80} for the monitored peaks in the xenon tests. All the numbers are given in hours. The control data sets have no speed up operation performed. The mixing data sets have been mixed with the steel ball for the indicated amount of minutes (0, 5 and 20) and then the red valve from figure 4.1 is opened.

Chapter 5

Measurement of helium

XENON1T employs PMTs to detect light signals generated by the scattering of dark matter particles with xenon nuclei. The PMTs are directly in contact with the liquid (bottom array) and gaseous xenon (top array). Helium, the lightest noble gas, is very volatile and has a small atomic radius, and it is known to diffuse easily. A high concentration of helium could penetrate inside the vacuum of the PMTs, get ionized and cause false signals. Hence, it is necessary to verify that the concentration of helium in the xenon inventory is low.

The analysis technique used for measuring xenon in chapter 3 is not sensitive to helium. Helium was used as a carrier gas for gas chromatography, hence it is not visible in a gas chromatograph. Mass spectrometry provides an alternative to measure helium in xenon.

In this chapter, the measurement of the concentration of helium in xenon is described. First, the employed experimental setup is shown. Then the measurement of the concentration in a sample of ReStoX gas phase (Q_{RSX}^{He}) is performed. Last, the measurement is repeated for a sample drawn after a dedicated distillation campaign to reduce the helium concentration of ReStoX gas phase (Q_{dRSX}^{He}).

5.1 Experimental setup

Figure 5.1 shows a scheme of the experimental setup. To measure the concentration, the Prisma Quadrupole Mass Spectrometer 200 (QMS) used in chapter 4 was employed. The QMS was operated again at a pressure of $p_{vac} \simeq 1 \times 10^{-6}$ mbar. The high pressure sensor covers the range up to 1 bar, while the low pressure sensor is more precise but can cover up to of 0.1 bar.

The ReStoX sample is stored in the volume between the valves colored in blue in figure 5.1. In order to avoid air contamination, the sample is stored in all three volumes between the valves, the middle volume being shielded by the two

surrounding ones and supposed to be the purest. The sample was taken from ReStoX gas phase at the same time the gas phase was measured with the gas chromatograph (see section 3.5.1).

To detect concentrations of helium of the order of ppb, a cold finger is installed. The cold finger consists of a stainless steel pipe blinded at one end.

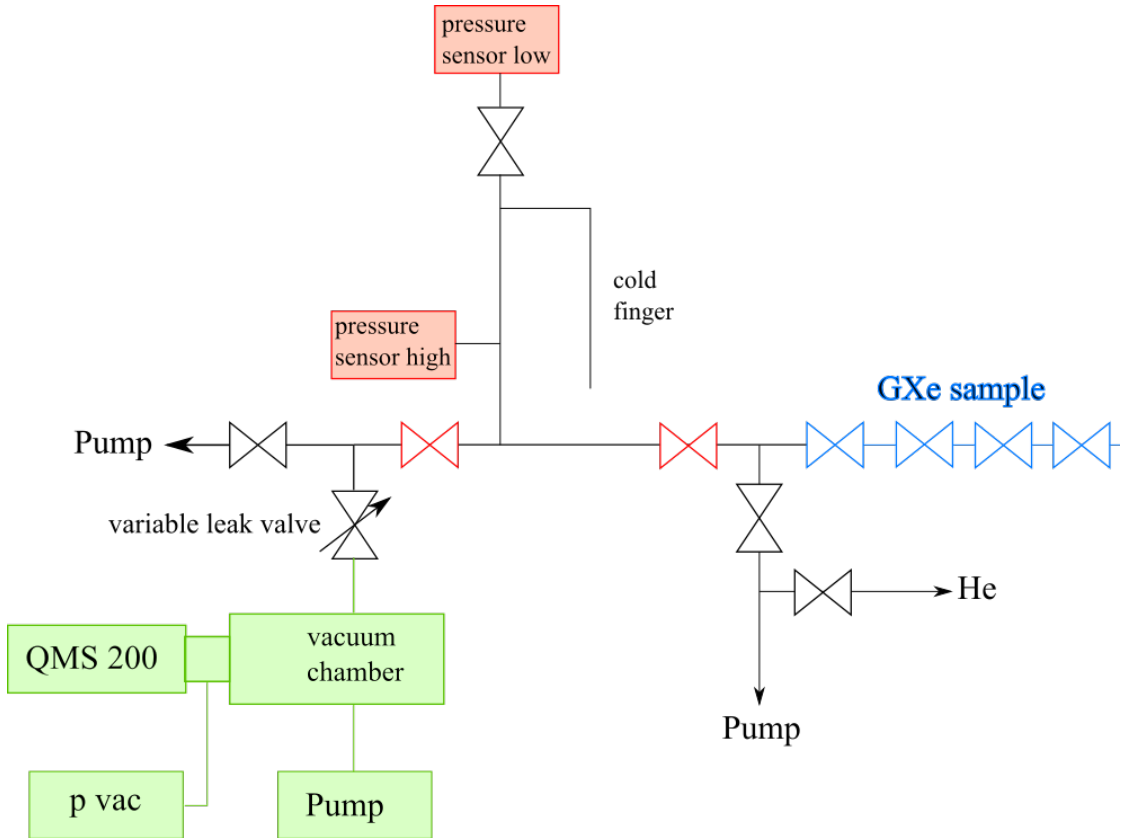


Figure 5.1: Scheme for measuring the helium concentration. The volume between the blue valves is called pipette and it is used to store the xenon for transportation.

5.2 First measurement

Since we are interested in the exact amount of impurities, an absolute calibration is needed. This was performed with a mixture of 74% xenon and 26% helium. The calibration sample was mixed filling helium in a bottle and then adding xenon until the partial pressures of the two gases give the ratio indicated above. A problem with this calibration method is that the response of the vacuum gauge at the vacuum chamber (p_{vac}) depends on the gas mixture [53]. Accounting to the

manufacturer, the effective pressure p_{eff} is

$$p_{eff} = K \cdot p_{vac} \quad (5.1)$$

where K is a correction coefficient that depends on the gas. The values for K are listed in [53]. For the two gases of interest, He and Xe, K is 5.9 and 0.4 respectively. This effect introduces a new systematic uncertainty which needs to be accounted for.

Before the beginning of the measurement, the opening of the leak valve was fixed to $p_{vac} = 1 \times 10^{-6}$. The valve was not moved for the other measurements in this section. Figure 5.2 shows the first measurement. There is already a visible peak at mass 4 amu. The evaluation of the area of the peaks have been done using the same method as in section 4.4. The area of the peaks has been found to be linear with p_{eff} at this order of magnitude.

To get the corrected concentration of helium, the correction of p_{eff} in equation 5.1 must be taken into account. For a mixture with 26% of helium the correction coefficient is 1.83. For a pure xenon signal, with helium concentration of the order $\mathcal{O}(100)$ ppm, the correction coefficient is 0.4, giving a total correction factor of 0.22. Ignoring the correction to p_{vac} , the measured helium concentration is (300 ± 10) ppm. Applying the correction factor, the corrected helium concentration is $Q_{RSX}^{He} = (66 \pm 2)$ ppm.

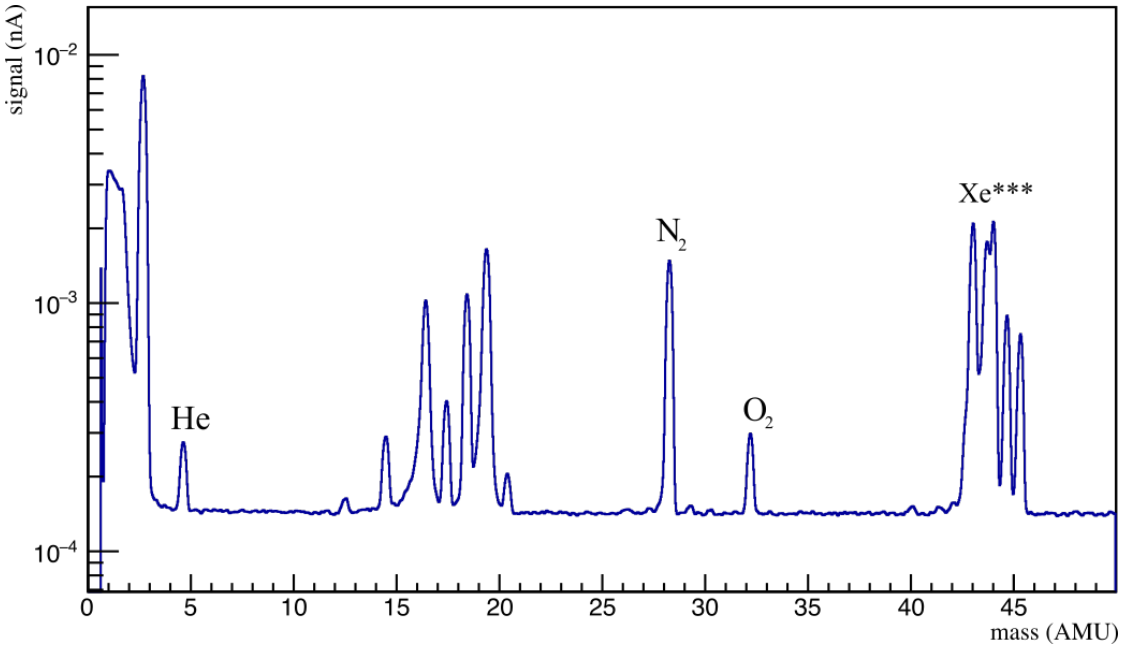


Figure 5.2: Mass spectrum of the measurement of ReStoX gas phase. The unlabelled peaks are part of the background.

After this first test, a second measurement applying liquid nitrogen to the cold finger is performed. The test has been carried out to validate the presence of the helium in the xenon sample and to study the performance of the system when the xenon is frozen.

After some minutes that liquid nitrogen is applied, the xenon signal drops below the sensitivity of the QMS, so we concluded that most of the xenon is trapped at the cold finger. The residual gas is composed mostly by helium (red in figure 5.3). After the measurement, the residual gas is pumped using the pump at QMS setup until the helium signal is below the sensitivity. The cold finger is then warmed up again, releasing the xenon. While the xenon signal was found to be consistent with the initial measurement, the peak at mass 4 amu now is absent (blue in figure 5.3).

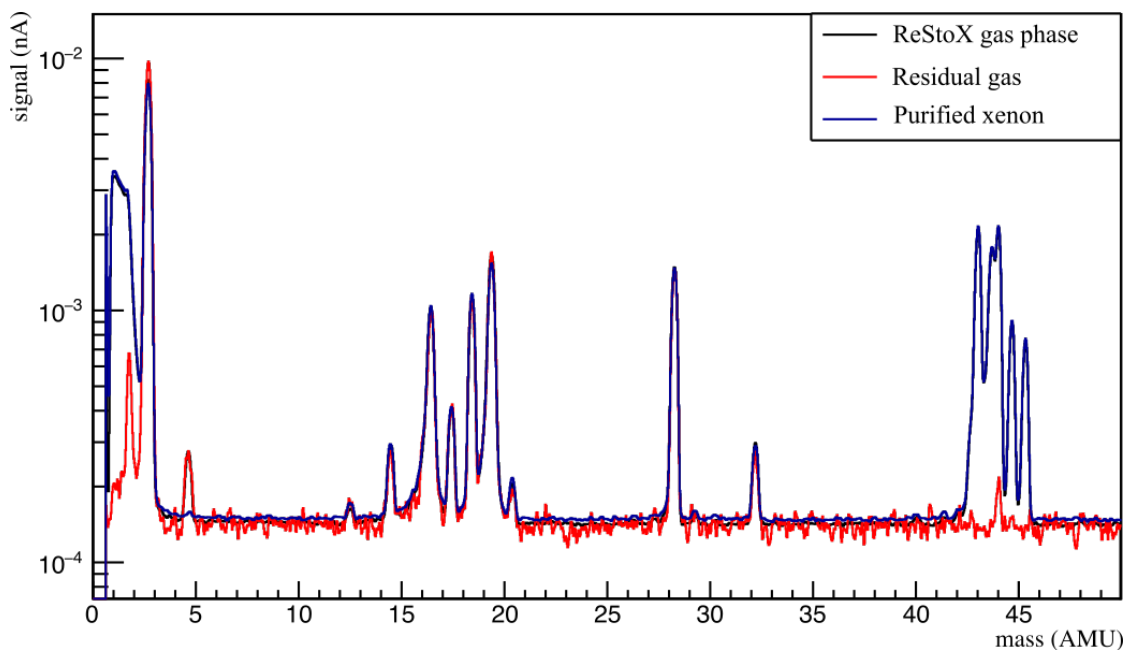


Figure 5.3: Mass spectrum of the measurement of ReStoX gas phase (black), the residual gas while the cold finger was frozen (red) and the purified xenon after the residual gas was pumped (blue). The helium peak is not present in the latter spectrum.

The latter test shows that the helium peak in the initial measurement is not an artifact of the system but a genuine signal. It also shows that the helium and the xenon signals are stable before, during (in the case of helium) and after (in the case of xenon) applying liquid nitrogen to the cold finger. This means that the peak size in a spectrum only depends on the partial pressure of the gases, and not on the overall pressure. This system can then be used to prepare a calibration gas at ppm level.

The measurement also shows that the concentration of helium in frozen xenon is negligible, and it hints that it is sufficient to distillate only the gas phase to purify the helium. Since the measured helium concentration is harmful for the PMTs, a distillation of ReStox gas phase was carried out.

ReStoX gas phase contains $\mathcal{O}(40)$ kg of xenon. The distillation was performed in a continuous loop with a flow of 3 kg/h at 1% offgas. Xenon is flown from the gas phase, fed to the distillation column and finally brought back to the gas phase. The total amount of xenon distilled is 225 kg, 5.6 times amount in the gas phase. A new sample is taken from ReStoX gas phase after the distillation and the results are presented in the next section.

5.3 Measurement after distillation

Between the two measurements, conditions of operation of the QMS have changed and, therefore, the background and the sensitivity of the QMS are different. Figure 5.4 shows a new background spectrum overlaid with the spectrum of ReStoX gas phase after distillation. The leak valve was set such that $p_{vac} = 8.2 \times 10^{-7}$ mbar and was not moved for the measurements in this section. The notable difference is the increased size of the bumps at masses below 4 amu. The tail of this noise feature now impairs the measurement of the peak at 4 amu.

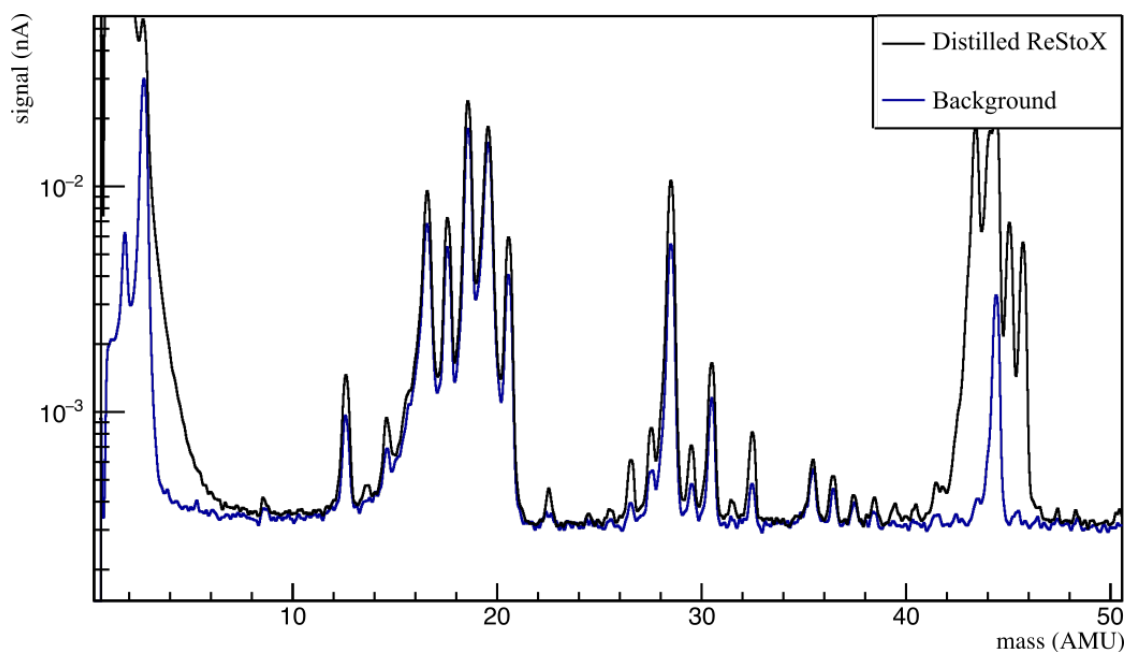


Figure 5.4: Background mass spectrum (blue) and ReStoX gas phase after distillation (black). Only the triple ionized xenon signal is visible on top of the background.

Even with the long tail, there is no visible helium peak in the spectrum. In order to confirm the absence of helium, the measurement has been repeated immersing the cold finger in liquid nitrogen. Figure 5.5 shows the spectrum of the residual gas (red) compared with the background (blue). The tail is not present anymore in the residual gas measurement and there is no visible peak at mass 4 amu. The helium concentration is below the sensitivity of the setup.

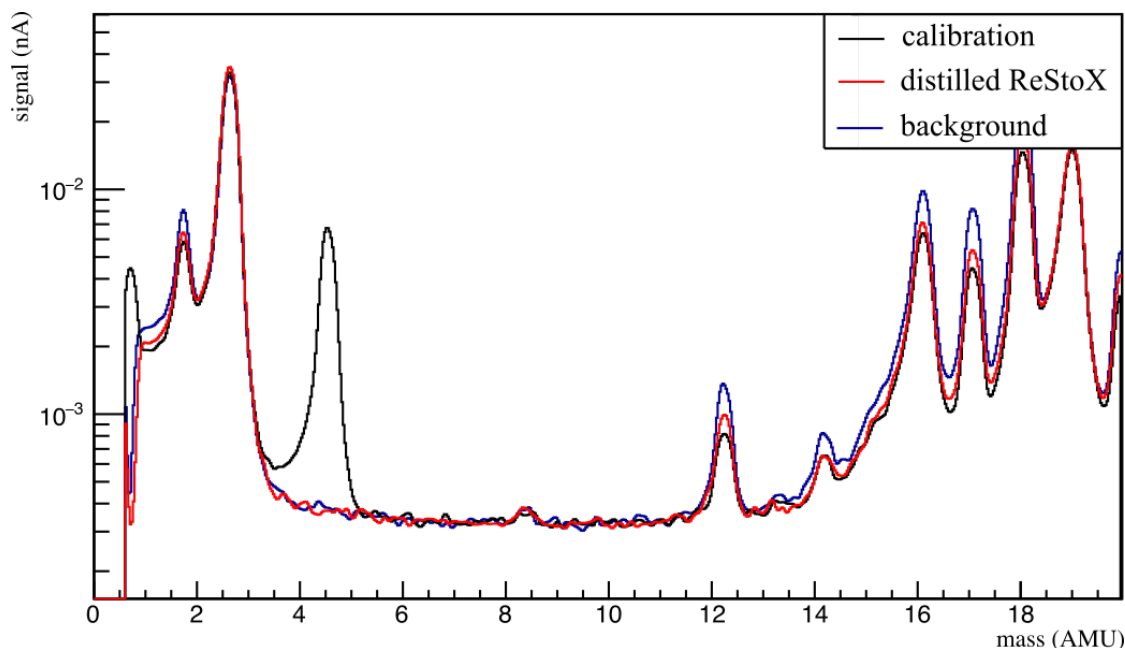


Figure 5.5: Comparison between the ReStoX gas phase after distillation (red) and the measured signal for a 320 ppm helium peak (black). The blue spectrum is the background.

In order to estimate the sensitivity of the QMS at this conditions of operation, a calibration measurement has been performed avoiding the systematics associated to the vacuum gauge measurements. The xenon has been purified with the same procedure as in section 5.2. The xenon was frozen in the cold finger and the residual gas phase was pumped for some minutes. The cold finger is then warmed up again to return the xenon at gaseous state.

Using this procedure, the volume between the red valves in figure 5.1 has been filled with purified xenon at $p_{low} = (22.5 \pm 0.6)$ mbar, then the xenon was frozen again. The same volume has been filled with helium at $p_{low} = (7.3 \pm 0.2) \times 10^{-3}$ mbar. The xenon is then warmed up, so that the helium concentration is (320 ± 10) ppm (red in figure 5.5).

To have a not null measurement, the peak area must be significantly bigger than the fluctuations of the background in the region of the peak. The region of the peak is found via the calibration measurement (as explained in section 4.4). To avoid the systematics uncertainties associated with the steeply falling baseline at mass 4 amu, this analysis is done on the frozen xenon measurement.

Both in the background and the frozen xenon measurement, it is possible to fit a line in the signal region. The fluctuation of the background are calculated by integrating the area above the line. These areas are then filled in a gaussian

distribution. It is possible to set a threshold, above which an area has 5% or less probability to be in the background distribution: this threshold determines the sensitivity. Using this technique and the last calibration to convert the area into a concentration, it is possible to estimate that the sensitivity is 4 ppm. Since there is no peak visible in the distilled ReStoX sample, the helium concentration Q_{dRSX}^{He} is lower than 4 ppm. This is an acceptable concentration, so the distillation procedure was successful.

Appendix A

Tables

Table of properties of the elements and compounds used in this work. T_f = freezing temperature at atmospheric pressure. T_b = boiling temperature at atmospheric pressure. σ = characteristic Lennard-Jones length. ϵ = characteristic Lennard-Jones energy.

Table A.1: Table of properties of most used elements and compounds. From ref [50]

Substance	Molecular weight cm ³ /g mol	T_f (K)	T_b (K)	σ (Å)	ϵ/k (K)
H ₂	2.016	13.83	20.27	2.827	59.7
He	4.003	2.15	4.3	2.551	10.22
Ne	20.180	24.56	27.07	2.82	32.8
CH ₄	16.043	90.69	111.66	3.758	148.6
H ₂ O	18.015	273.15	373.15	2.641	809.1
N ₂	28.014	63.15	77.35	3.798	71.4
O ₂	31.999	54.36	90.17	3.467	106.7
Ar	39.948	83.8	87.27	3.542	93.3
Kr	83.800	115.77	119.74	3.655	178.9
Xe	131.290	161.25	165.01	4.047	231

Appendix B

Mass Spectrometry

Mass Spectrometry is a popular analysis technique for measuring the concentration of individual components in a gas mixture. The sample gas is diluted and ionized through electron bombardment. The ions are then separated using a magnetic field that select a specific mass to charge ratio (m/e).

The mass spectrometer employed is a Pfeiffer Vacuum Prisma Quadrupole Mass Spectrometer 200 (QMS 200) [54]. Figure B.1 shows the setup of a quadrupole mass spectrometer. The mass filter consists of four parallel rods arranged to form a square. Each pair of opposite rods have positive or negative charge. Inside the rods, an electric field with both a DC portion and an AC portion is applied. The ions are injected with approximately equal energy at one end of the rods (z axis). The quadrupole field deflects the ions on the x y plane, causing them to describe helical trajectories. If the radius is bigger than the field radius r_0 , the ions discharge on the rods, otherwise they pass through the filter and reach the detector. Changing the amplitude of the DC and AC field, it is possible to modify the radius of the orbit of the ions thus selecting particles with different masses.

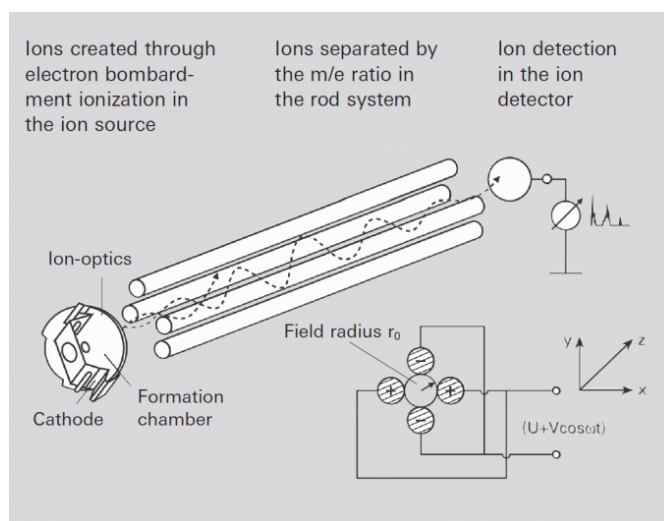


Figure B.1: Scheme of a quadrupole mass spectrometer [54].

The QMS M200 is equipped with an cross beam ion source (see figure B.2). Electrons of pre-selectable energy (0 - 120 eV) are formed in area (3) from one of the two tungsten filaments (1). The Wehnelt cylinder (4) prevents the electrons from scattering in the environment. The beam of molecules and atoms comes from above, is ionized in (7) and are channeled at the bottom to reach the mass filter.

It is possible that one molecule is ionized more than once. In this case, the ratio $m/(n \cdot e)$ is selected, where n is the number of times one molecule is ionized. This effect causes the appearance of peaks at a mass which is one half or one third of the original isotopes' mass.

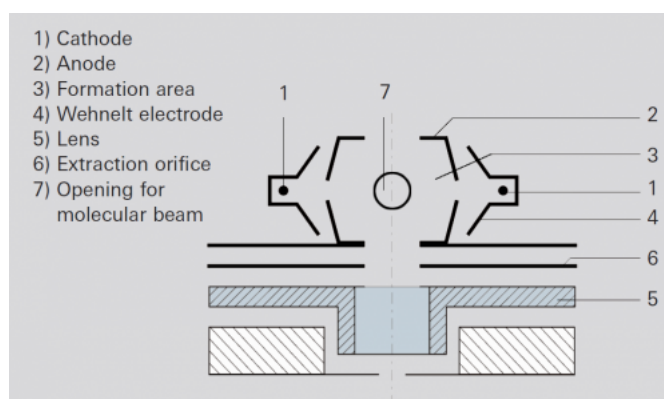


Figure B.2: Scheme of the cross beam ion source [54].

The QMS M200 is equipped with two detectors: a faraday cup detector and a continuous dynode secondary electron multiplier (C-SEM). For all the measure-

ments, the C-SEM has been used since it is more sensitive. The scheme is shown in figure B.3. The ions from the quadrupole field are converted in electrons through a dynode and gathered in a glass tube. In the interior of the tube a uniform voltage is created, which generates an avalanche of electrons (with an amplification factor of 10^6).

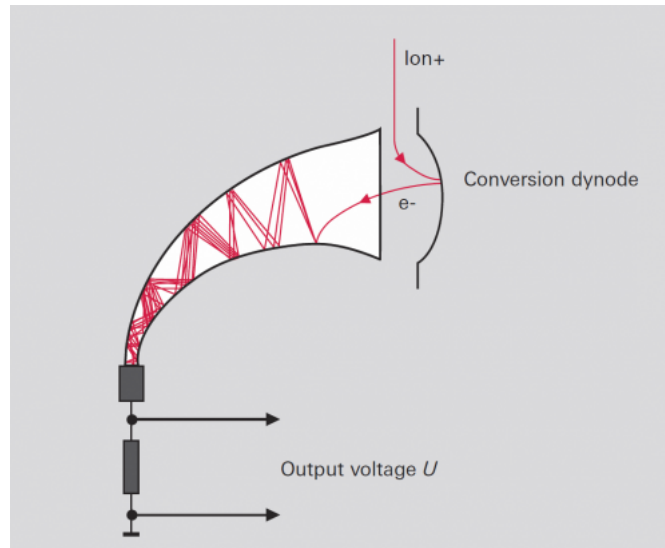


Figure B.3: Scheme of the C-SEM detector [54].

Bibliography

- [1] F. Zwicky. “Spectral displacement of extra galactic nebulae”. In: *Helv. Phys. Acta.* 111.6 (1933).
- [2] K. G. Begeman, A. H. Broeils, and R. H. Sanders. “Extended rotation curves of spiral galaxies - Dark haloes and modified dynamics”. In: *Monthly Notices of the Royal Astronomical Society* 249 (1991), pp. 523–537.
- [3] G. Bertone. *Particle Dark Matter*. Cambridge University Press, 2010.
- [4] C. Alcock et al. “The MACHO project: Microlensing results from 5.7 years of LMC observations”. In: *The Astrophysical Journal* 542 (2000), pp. 281–307.
- [5] Marusa Bradac et al. “Strong and weak lensing united. 3. Measuring the mass distribution of the merging galaxy cluster 1E0657-56”. In: *The Astrophysical Journal* 652 (2006), pp. 937–947.
- [6] *Artistic image of the bullet cluster*. NASA. URL: <http://apod.nasa.gov/apod/ap060824.html>.
- [7] Douglas Clowe et al. “A direct empirical proof of the existence of dark matter”. In: *The Astrophysical Journal* 648 (2006), pp. L109–L113.
- [8] D. J. Fixsen. “The Temperature of the Cosmic Microwave Background”. In: *The Astrophysical Journal* 707 (Dec. 2009), pp. 916–920.
- [9] C. L. Bennett et al. “Nine-year Wilkinson Microwave Anisotropy Probe (WMAP) Observations: Final Maps and Results”. In: *The Astrophysical Journal* 208, 20 (2013).
- [10] P. A. R. Ade et al. “Planck 2013 results. I. Overview of products and scientific results”. In: *Astron. Astrophys.* 571 (2014), A1.
- [11] Claude Amsler et al. “Review of Particle Properties”. In: *Phys. Lett. B* 667.1-5 (2008), pp. 1–6.
- [12] V. Springel, C. S. Frenk, and S. D. M. White. “The large-scale structure of the Universe”. In: *Nature* 440.7088 (2006), pp. 1137–1144.
- [13] Mordehai Milgrom. “MOND theory”. In: *Can. J. Phys.* 93.2 (2015), pp. 107–118.

- [14] T. H. Randriamampandry and C. Carignan. “Galaxy mass models: MOND versus dark matter haloes”. In: *Monthly Notices of the Royal Astronomical Society* 439 (2014), pp. 2132–2145.
- [15] *Particle Data Group Website*. URL: <http://pdg.lbl.gov/>.
- [16] Y. Fukuda et al. “Evidence for oscillation of atmospheric neutrinos”. In: *Phys. Rev. Lett.* 81 (1998), pp. 1562–1567.
- [17] Toby Falk, Keith A. Olive, and Mark Srednicki. “Heavy sneutrinos as dark matter”. In: *Phys. Lett.* B339 (1994), pp. 248–251.
- [18] Patrick J. Fox et al. “Missing Energy Signatures of Dark Matter at the LHC”. In: *Phys. Rev.* D85 (2012), p. 056011.
- [19] H. Baer and Xerxes Tata. “Dark matter and the LHC”. In: *Physics at the Large Hadron Collider*. Ed. by Amitava Datta et al. 2009, pp. 179–203.
- [20] R. Abbasi et al. *Multiyear search for dark matter annihilations in the Sun with the AMANDA-II and IceCube detectors*. Feb. 2012.
- [21] W. B. Atwood et al. “The Large Area Telescope on the Fermi Gamma-Ray Space Telescope Mission”. In: *The Astrophysical Journal* 697 (June 2009), pp. 1071–1102.
- [22] V. Barger et al. “PAMELA and dark matter”. In: *Phys. Lett.* B672 (2009), pp. 141–146.
- [23] J. D. Lewin and P. F. Smith. “Review of mathematics, numerical factors, and corrections for dark matter experiments based on elastic nuclear recoil”. In: *Astropart. Phys.* 6 (1996), pp. 87–112.
- [24] Riccardo Catena and Piero Ullio. “A novel determination of the local dark matter density”. In: *JCAP* 1008 (2010), p. 004.
- [25] J. Billard, L. Strigari, and E. Figueroa-Feliciano. “Implication of neutrino backgrounds on the reach of next generation dark matter direct detection experiments”. In: *Phys. Rev.* D89.2 (2014), p. 023524.
- [26] E. Aprile et al. “Physics reach of the XENON1T dark matter experiment.” In: *Journal of Cosmology and Astroparticle Physics* 2016.04 (2016), p. 027.
- [27] C. Savage et al. “Compatibility of DAMA/LIBRA dark matter detection with other searches”. In: *Journal of Cosmology and Astroparticle Physics* 0904 (2009), p. 010.
- [28] R. Agnese et al. “Silicon Detector Dark Matter Results from the Final Exposure of CDMS II”. In: *Phys. Rev. Lett.* 111.25 (2013), p. 251301.
- [29] R. Agnese et al. “Search for Low-Mass Weakly Interacting Massive Particles with SuperCDMS”. In: *Phys. Rev. Lett.* 112.24 (2014), p. 241302.

- [30] M. Xiao et al. “First dark matter search results from the PandaX-I experiment”. In: *Science China Physics, Mechanics and Astronomy* 57.11, 2024 (2014), p. 2024.
- [31] P. Agnes et al. “Results from the first use of low radioactivity argon in a dark matter search”. In: *Phys. Rev. D* 93.8 (2016), p. 081101.
- [32] D. S. Akerib et al. “Improved Limits on Scattering of Weakly Interacting Massive Particles from Reanalysis of 2013 LUX Data”. In: *Phys. Rev. Lett.* 116.16 (2016), p. 161301.
- [33] E. Aprile et al. “First Results from the XENON10 Dark Matter Experiment at the Gran Sasso National Laboratory”. In: *Phys. Rev. Lett.* 100 (2 Jan. 2008), p. 021303.
- [34] E. Aprile et al. “Dark Matter Results from 225 Live Days of XENON100 Data”. In: *Phys. Rev. Lett.* 109 (2012), p. 181301.
- [35] E. Aprile and T. Doke. “Liquid Xenon Detectors for Particle Physics and Astrophysics”. In: *Rev. Mod. Phys.* 82 (2010), pp. 2053–2097.
- [36] Kaixuan Ni and Laura Baudis. “Direct Dark Matter Searches with CDMS and XENON”. In: *Adv. Space Res.* 41 (2008), pp. 2019–2023.
- [37] E. Aprile et al. “The XENON100 dark matter experiment”. In: *Astroparticle Physics* 35 (Apr. 2012), pp. 573–590.
- [38] E. Aprile et al. “Likelihood Approach to the First Dark Matter Results from XENON100”. In: *Phys. Rev. D* 84 (2011), p. 052003.
- [39] E. Aprile et al. “Analysis of the XENON100 Dark Matter Search Data”. In: (2012). arXiv: 1207.3458v3 [astro-ph.IM].
- [40] E. Aprile et al. “Conceptual design and simulation of a water Cherenkov muon veto for the XENON1T experiment”. In: *JINST* 9 (2014), p. 11006.
- [41] Dongming Mei and A. Hime. “Muon-induced background study for underground laboratories”. In: *Phys. Rev. D* 73 (2006), p. 053004.
- [42] *Earth fact sheet*. NASA. URL: nssdc.gsfc.nasa.gov/planetary/factsheet/earthfact.html.
- [43] Y. Dong. “Study of the automatic controls of the ReStoX system for the XENON1T experiment”. Master thesis. University of Nantes, 2014.
- [44] C. Hasterok. “In preparation”. PhD thesis. University of Heidelberg, 2017.
- [45] H. M. McNair and J. M. Miller. *Basic Gas Chromatography*. 2nd ed. Wiley, 2009.

- [46] H Cai, W. E. Wentworth, and S. D. Stearns. “Characterization of the Pulsed Discharge Electron Capture Detector”. In: *Anal. Chem.* 68 (7) (1996), pp. 1233–1234.
- [47] S. Lindemann. “Intrinsic ^{85}Kr and ^{222}Rn Backgrounds in the XENON Dark Matter Search”. PhD thesis. University of Heidelberg, 2013.
- [48] S. Chapman and T. G. Cowling. *The Mathematical theory of non-uniform gas*. 3rd ed. Cambridge University Press, 1999.
- [49] J. Crank. *The Mathematics of diffusion*. 3rd ed. Oxford University Press, 1975.
- [50] B. E. Poling, J. M. Prausnitz, and J. P. O’Connell. *The Properties of Gases and Liquids*. 5th ed. Oxford University Press, 2001.
- [51] Eric W. Weisstein. *Heat Conduction Equation*. MathWorld-A Wolfram Web Resource. URL: <http://mathworld.wolfram.com/HeatConductionEquation.html>.
- [52] *Variable Leak Valve manual*. Agilent Technologies. URL: <https://www.agilent.com/cs/library/usermanuals/public/Variable%20leak%20valve.pdf>.
- [53] *Compact FullRange Gauge manual*. Pfeiffer Vacuum. URL: http://www.idealvac.com/files/ManualsII/Pfeiffer_PBR260_Operating_Instructions.pdf.
- [54] *Pfeiffer Vacuum Website*. Pfeiffer Vacuum. URL: <http://www.pfeiffer-vacuum.com/en/>.

Acknowledgement

I would like to thank all the people who enabled me to write this thesis at Max-Planck-Institut fuer Kernphysik in Heidelberg. Foremost, I would like to thank Prof. Manfred Lindner for the opportunity to work in the XENON collaboration and for his support. Special mention goes to the Erasmus+ program, which allowed me and many more students to travel in Europe.

I would like to thank all the members of the XENON group at the Max-Planck-Institut, for supporting me during all circumstances. In particular, I thank Dr. Hardy Simgen for his suggestion and giving me the opportunity to work at LNGS and Dr. Teresa Marrodan Undagoitia for her support during this work. Special thanks go to Dr. Sebastian Lindemann, for his help but foremost for his endless patience and answering all my “stupid” questions. I would like to thank also Constanze Hasterock for enabling me to collaborate with her, and for trusting me with her “baby”. I would also like to thank Stefan Bruenner for his help and the long walks on the mountains.

My stay would not have been amazing without all the people I met. I would like to thank Daniel, Daniele, Helena, Hyoyin and everyone else who made this time fantastic. I would also like to thank Riccardo for all the remote conversation. Finally, I would like to thank my family, especially my parents, who gave me endless support in all my life decisions.